İSTANBUL TECHNICAL UNIVERSITY ★ INSTITUTE OF SCIENCE AND TECHNOLOGY

PISTON SECONDARY DYNAMICS
AND SKIRT LUBRICATION

M.Sc. Thesis by
Özgür GÜNELSU

503031013

Date of submission : **8 May 2006**

Date of defence examination : **15 June 2006**

Supervisor (Chairman) : **Assist. Prof. Dr. Özgen AKALIN**
Members of the Examining Committee : **Prof.Dr. Metin ERGENEMAN (İ.T.Ü.)**

Prof.Dr. İrfan YAVAŞLIOL (Y.Ü.)

JUNE 2006

İSTANBUL TEKNİK ÜNİVERSİTESİ ★ FEN BİLİMLERİ ENSTİTÜSÜ

PİSTON İKİNCİL DİNAMİĞİ VE ETEK YAĞLAMASI

YÜKSEK LİSANS TEZİ

Özgür GÜNELSU

503031013

Tezin Enstitüye Verildiği Tarih : 8 Mayıs 2006

Tezin Savunulduğu Tarih : 15 Haziran 2006

Tez Danışmanı : Y.Doç.Dr. Özgen AKALIN

Diğer Jüri Üyeleri : Prof.Dr. Metin ERGENEMAN (İ.T.Ü.)

Prof.Dr. İrfan YAVAŞLIOL (Y.T.Ü.)

HAZİRAN 2006

ACKNOWLEDGEMENT

First of all, I'd like to thank my supervisor Dr. Akalın for not only his academic support, but also for his sincere efforts to mentally, psychologically and financially keep me in this study.

This study was a part of the project named as "Reducing the Piston Assembly Friction Losses in Internal Combustion Engines (İçten Yanmalı Motorlarda Piston Grubu Sürtünme Kayıplarının Azaltılması)" with the project number 104M274, which was supported by TÜBİTAK (The Scientific and Technological Research Council of Turkey). Financial support through this project is gratefully acknowledged and I declare that none of the opinions, established ideas or conclusions in this thesis report is the official opinion, idea or conclusion of TÜBİTAK.

Also, I appreciate the partial financial aid from OTAM for a period of this study, and permanent support of the OTAM staff, especially Mr. Yunus Canlı, gave me by creating a friendly atmosphere both inside and outside the campus.

In addition, I would like to thank my close friends, Fatih and İsmail for their three-years-lasting hospitality.

At last but not least, the most special thanks go to my parents Gülşen and Cevat for their patience and their great support to my insistence in academic studies as well as to all my twenty-six years.

TABLE OF CONTENTS

ABBREVIATIONS

ATS	:	Anti-thrust side
BDC	:	Bottom dead center
CA	:	Crank angle
CCD	:	Charge-coupled device
CPU	:	Central processing unit
DLC	:	Diamond-like carbon
EHD	:	Elastohydrodynamic
FE	:	Finite element
FTDC	:	Firing top dead center
ICE	:	Internal combustion engine
JFO	:	Jakobsson-Floberg-Olsson
LHS	:	Left hand side
RHS	:	Right hand side
PSD	:	Piston secondary dynamics
PSM	:	Piston secondary motion
SAE	:	Society of Automotive Engineers
TDC	:	Top dead center
TS	:	Thrust side

LIST OF TABLES

LIST OF FIGURES

Page No.

LIST OF SYMBOLS

a_{pX}	:	Piston center of mass axial acceleration
a_{pZ}, e_{CM}	:	Piston center of mass lateral acceleration
e_t, e_b, e_{CM}	:	Piston top, bottom and mass center eccentricities
h	:	Film thickness
h_{max}	:	Inlet supply film thickness
i, j	:	Nodal coordinates
i_c, j_c	:	Nodal coordinates of cavitation boundary
m, n	:	Mesh dimensions
m_b	:	Connecting rod mass
m_p	:	Piston mass
p	:	Pressure
p_c	:	Asperity contact pressure
p_L, p_T	:	Leading and trailing edge pressures
r	:	Piston radius
r_c	:	Crank radius
x_1, x_i	:	Inlet location
x_2, x_p	:	Film rupture location
x_3, x_i	:	Film reformation location
z_{CM}, z_P	:	Location of piston mass center and pin axis
A_{bX}, A_{bZ}	:	Connecting rod mass center axial and lateral accelerations
AW, AE, AS, AN, AP, S	:	Coefficients of discretized Reynolds equation
C_{BP}	:	Distance form connecting rod mass center to small end
C_{MB}	:	Distance from connecting rod mass center to big end
F_f	:	Piston skirt friction force
F_g	:	Gas force
F_h	:	Piston skirt normal force
F_{MX}, F_{MZ}	:	Connecting rod big end force components
F_{rX}, F_{rZ}	:	Pin force components
H, H_σ	:	Non-dimensional local film thickness
I_b	:	Connecting rod moment of inertia
I_p	:	Piston moment of inertia
L	:	Effective skirt length
M_f	:	Moment due to piston skirt friction force
M_h	:	Moment due to piston skirt normal force
M_{pin}	:	Moment due to pin friction
P	:	Non-dimensional pressure
P_1, P_2	:	Non-dimensional leading and trailing edge pressures
R	:	Cylinder radius
T	:	Non-dimensional time
U	:	Piston axial velocity
U^*	:	Non-dimensional piston axial velocity

V_{r1}, V_{r2}	:	Surface roughness variance ratios
X, Y	:	Non-dimensional coordinates
α	:	Piston tilt angle
β	:	Squeeze film factor
ϕ	:	Connecting rod tilt angle
ϕ_c	:	Contact factor
ϕ_{fs}, Φ_{fs}, ϕ_f	:	Correction terms
ϕ_s, Φ_s	:	Shear flow factors
ϕ_x, ϕ_y	:	Pressure flow factors
γ	:	Surface roughness orientation factor
μ	:	Dynamic viscosity
μ_f	:	Coefficient of friction
θ_{lub}	:	Coordinate of skirt lubricated area boundary
σ	:	Composite surface roughness
σ^*	:	Non-dimensional surface roughness
σ_1, σ_2	:	Surface roughness of sliding surfaces
τ	:	Crank angle
ω	:	Crank speed

PISTON SECONDARY DYNAMICS AND SKIRT LUBRICATION

SUMMARY

This study aims to determine the behavior of an oil-lubricated piston reciprocating inside a cylinder in the context of its lateral motion, and to state its contribution to total piston assembly friction. For this purpose, a detailed model was constructed and a MATLAB code was written solving secondary motion of a piston in mixed lubrication. In regard to its effects on the operation of the piston, primary importance was attached to skirt lubrication. Effects of surface roughness of both skirt and liner were taken into account using the modified form of Reynolds equation with pressure and shear flow factors. An asperity contact model was introduced for the effect of solid-to-solid contact of surface asperities. In addition, continuity of lubricant film between skirt and liner surfaces was investigated. Reynolds flow separation approach was used to determine film rupture boundary for the two-dimensional flow of lubricant. Results of the simulations were compared to those of previous theoretical and experimental studies. Effects of variation of design parameters, such as nominal clearance, skirt barrel profile, surface texture and material and lubricant properties were compared and discussed. Subsequently, the model was optimized for further use as a tool to predict friction, wear and lubrication properties of power cylinder components.

PİSTON İKİNCİL DİNAMİĞİ VE ETEK YAĞLAMASI

ÖZET

Bu çalışmanın amacı öteleme hareketi yapan bir pistonun silindir içindeki davranışını yanal hareketi bağlamında incelemektir ve toplam piston grubu sürtünmesine olan katkısını belirlemektir. Bu amaçla detaylı bir model oluşturulmuş ve karma yağlama rejiminde çalışan bir pistonun ikincil dinamiği çözümü için bir MATLAB kodu yazılmıştır. İkincil dinamiğine olan etkileri bakımından, etek yağlamasına birincil derecede önem gösterilmiştir. Basınç ve kayma akış katsayıları eklenerek tadil edilmiş olan Reynolds denklemi kullanılarak piston ve silindirin yüzey pürüzlülüklerinin etkisi hesaba katılmıştır. Bir pürüz teması modeli esas alınarak katı sütrünmenin etkileri de dikkate alınmıştır. Buna ek olarak, yüzeyler arasında oluşan film tabakasının devamlılığı incelenmiştir. İki boyutlu akışta, yağ filminin kopma sınırının belirlenmesinde Reynolds akış ayrılması yaklaşımından yaralanılmıştır. Ulaşılan sonuçlar daha önceki teorik ve deneysel çalışmalarda elde edilmiş sonuçlarla karşılaştırılmıştır. Yüzeyler arasındaki nominal boşluk, etek fıçı profili, yüzey dokusu ve malzeme ve yağ özellikleri gibi tasarım parametrelerinin değişimlerinin etkileri tartışılmıştır. Sonuçların değerlendirilmesinin ardından modelin ileriki çalışmalarda piston-silindir parçalarının sürtünme, aşınma ve yağlama özelliklerinin belirlenmesi için bir araç olarak kullanılmasına yönelik optimizasyonuna gidilmiştir.

1 INTRODUCTION

In reciprocating piston machines such as conventional internal combustion engines and reciprocating compressors, beside the reciprocation inside the cylinder in the axial direction, piston also moves in the lateral direction causing piston secondary motion. Considering the clearance between piston skirt and cylinder liner, the displacement of the piston in the lateral direction is very small. However, the performance is greatly affected from secondary motion of the piston, since it determines the conditions of lubrication. Depending on the lubrication quality, engine friction loss in piston–piston ring-cylinder liner assembly that constitutes 25-50% of the total mechanical losses in an internal combustion engine, affects the engine's mechanical efficiency. Figure 1.1 shows utilization of power gained from a medium size passenger car engine [1]. Furthermore, lubrication has significant effects on fuel economy, oil consumption, exhaust emissions, durability and noise emission.

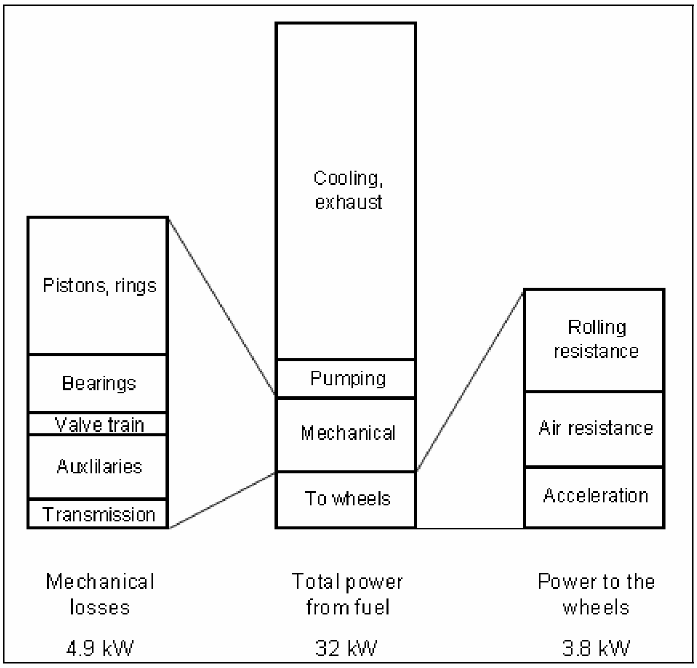

Figure 1.1 : Fuel energy utilization for a medium size passenger car during an urban cycle [1]

Piston secondary dynamics also plays an important role in noise emission. When the lateral speed of the piston is over certain values as it approaches the cylinder wall, oil film fails to cushion the piston skirt and it hits the bore causing piston slap.

Some design parameters such as piston pin offset, crank offset, quality of the lubricated surfaces and oil characteristics are worth mentioning for the smooth operation of piston in the context of its secondary motion.

1.1 Effects of Piston Secondary Motion on Engine Performance

Friction loss in piston-cylinder assembly is one of the major factors that reduce the mechanical efficiency of a power cylinder system. By providing a lubricant film between piston surfaces and cylinder liner, friction is tried to be kept at minimum values. However, since piston is subjected to a transient motion throughout a complete crank cycle, it is difficult to maintain a continuous film all over the piston skirt surface. Therefore piston design should be optimized in order to minimize the overall friction loss for a complete crank cycle, at every engine load and speed.

Wear is another parameter that should be considered during design stage for increased durability. Even during the operation of the piston with full lubricant film, viscous wearing occurs. However it is insignificant when compared to wear during dry contact. In other words, it is the rupture of fluid film between the surfaces that causes harmful wear of piston skirt and rings.

Film rupture can be avoided by having large clearance filled with high amount of lubricant, but in this case the problem of excessive oil consumption arises. One of the mechanisms that give rise to oil consumption is the oil-throw off from the top ring. While the piston is moving towards TDC, top ring on an ICE piston makes use of the oil left on the cylinder wall during the movement of the piston towards BDC. If the fluid film on the cylinder wall is thicker than the instantaneous clearance between ring and bore, the ring scrapes the excessive oil. Some of the oil accumulated on the ring escapes to the combustion chamber under the effect of high acceleration. As the clearance increases, the extent of piston’s capability to move in the lateral direction and the amount of oil scraped increase. High oil consumption is also undesired since it makes the control of exhaust emissions more difficult.

Therefore oil consumption in the piston-piston ring-cylinder assembly is one of the major design criteria.

Piston secondary dynamics also plays an important role in noise emission. When the lateral speed of the piston is over certain values as it approaches the cylinder wall, oil film fails to cushion the piston skirt and it hits the bore causing piston slap.

1.2 Parameters Affecting Piston Secondary Motion

The parameters affecting piston secondary motion can be investigated under three topics:

- Geometry
- Lubrication characteristics
- Elastic and thermal deformations

Geometry is the major parameter since it also determines the quality of lubrication and the extent of deformations with material properties. Geometric properties of primary importance are radial clearance, piston skirt length and barrel profile, pin and crank offset.

Radial clearance factor has already been discussed in the previous section, but barrel-shaped profile is not mentioned. Barrel shape of the lubricated surfaces provides a convergent passage during both upstroke and downstroke. This convergent passage is the major characteristic that forces the lubricant film to develop pressure.

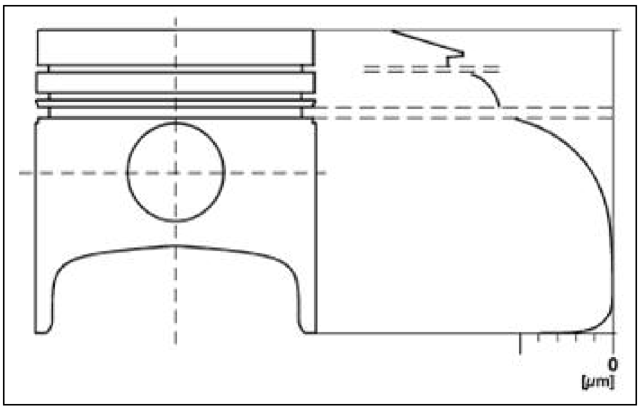

Figure 1.2 : Barrel-shaped piston skirt

Piston skirt maintains the smooth operation of the piston and rings by keeping piston tilt at low values. In addition, skirt provides a large surface for the support of lubricant film. Increasing the skirt length reduces the tilt and increases the load carrying capacity of the lubricant. However, it also increases the friction force and piston mass. Therefore it should be taken as an optimization problem.

Offsetting the pin or crank axes from the cylinder axis, are two of the methods two smoothen piston lateral motion. Due to varying gas pressure acting on piston top during the cycle, higher lateral forces are generated on the piston pin in one direction. A crankshaft offset towards anti-thrust side (Figure 1.3), leads to lower thrust, and higher anti-thrust side forces, in addition to slight improvement in combustion performance of internal combustion engines. Offsetting the pin axis changes the moment on the piston due to gas pressure and is a helpful design application to prevent excessive tilt of the piston.

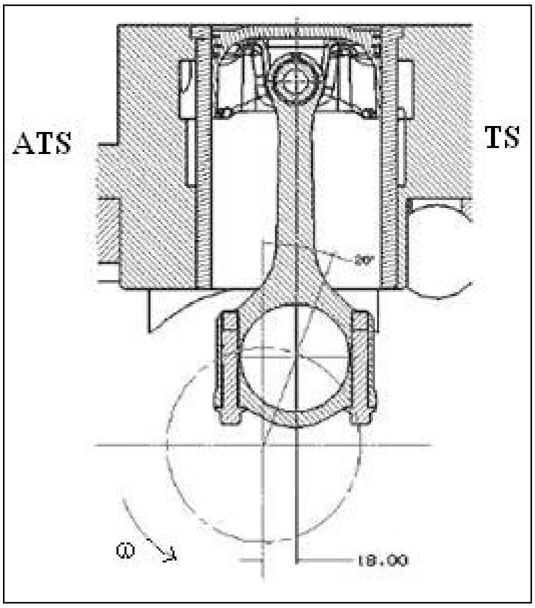

Figure 1.3 : Single-cylinder offset crankshaft design [28]

In lubrication quality, side clearance, barrel profile, surface finish and oil properties are important parameters. Side clearance and barrel profile have already been discussed above.

Asperities on the lubricated surfaces are in the orders of one hundredth of microns. These microscale roughness characteristic does not affect the lubrication quality for most part of the operation in applications in which nominal clearance values are over 10 microns. However, even tough there is not sufficient theoretical studies on the subject, experimental evidence is present that macroscale surface finish applications such as honing, coating or laser surface texturing provide considerable improvement in lubrication characteristics. Microscale surface asperities are effective in relatively small clearance applications as it is usually the case in small compressors. These microscale asperities, to some extent, aids hydrodynamic load carrying capacity by acting as barriers to the flow, but in friction point of view, especially in mixed and boundary lubrication regimes, they cause an increase in the power loss. Since microscale roughness cannot be avoided, it should be taken into consideration in lubrication applications.

Viscosity is the main characteristic determining the damping and frictional behavior of the lubricant. Decreasing the viscosity is advantageous for frictional performance; however it decreases damping, and thus load carrying capacity of the lubricant.

1.3 Literature Survey

1.3.1 Studies on Piston Secondary Dynamics and Skirt Lubrication

In the early studies of piston secondary dynamics, the piston was rigid and not lubricated. Lubrication effects and elastic deformations are gradually added to the models.

Greenwood and Tripp [2] developed the asperity contact model for two rough surfaces. Most models used to consider one of the contacting surfaces to be smooth. Elastic deformations of the asperities were also taken into account in the model.

Patir and Cheng [3,4] modified the Reynolds Equation adding the effect of three-dimensional roughness on hydrodynamic lubrication. They inserted pressure and shear flow factors and a factor for the extent of combined roughness of both surfaces into the equation. Effects of directionality of the surface patterns were also considered in the determination of flow factors.

Modified Reynolds equation was used by Zhu et al. [5] in the analysis of piston skirts in mixed lubrication. In this study, flow factors were defined in terms of surface waviness and roughness parameters, based on a geometrical model approximating the surface profile of a piston as sawtooth-shaped transversely-oriented identical waves and asperities. For the case of contact of surfaces, wavy and asperity contact pressures were discussed considering elastic deformations, but deformations were not included in the solution in this first part of the study.

Coulomb friction was assumed for the boundary film lubrication in possible solid-to-solid contact between piston skirt and cylinder bore.

A comprehensive skirt lubrication model was constructed by Keribar and Dursunkaya [6] for further use in a piston secondary dynamics analysis. Mixed lubrication was modeled without surface roughness effects on flow, using average Reynolds equation. Elastic deformations can be included in the solution as an input. In order to take the oil starvation into account, a parameter called the extent of lubrication was also used as an input and Reynolds equation was modified by a coordinate transformation for partially-flooded cases. Cavitation was treated by half-Sommerfeld condition as in fully-flooded case, even in partially-flooded lubrication conditions. This model was then coupled to a secondary dynamics model consisting of two parts for conventional and articulated piston assemblies and described by Dursunkaya and Keribar [7]. In this study, wristpin hydrodynamic and boundary lubrication and its motion within its bearing were also analyzed. To reduce the CPU time, a technique equivalent to the inverse of the “mobility map” scheme (impedance maps), often utilized in bearing analysis, was used: the hydrodynamic and contact pressure calculations for the pin are first carried out in a pre-processing code, and then inserted into the secondary dynamics model. Later on, Dursunkaya et al. [8] used these coupled models and presented the results making comparisons between elastic and rigid skirts and between conventional and articulated pistons.

Wong et al. [9] investigated piston secondary motion and piston slap in partially-flooded elastohydrodynamic skirt lubrication. They used modified Reynolds equation of Patir and Cheng [3] with the flow factors of Zhu et al. [5]. Partial lubrication was dealt by setting the hydrodynamic pressure to ambient pressure at the starvation points where the clearance gets higher than a reference value. For ring forces, a basic model was created and pre-processed. Negative clearance issue, which is caused by piston diameters larger than the bore diameter during normal operating conditions after the piston is fit cold into the cylinder, was prevented by setting a minimum clearance value at each grid point at the start of the iteration and continuing the iteration until non-negative clearance values are reached. Later, Mansouri and Wong [10] developed this model incorporating the effects of piston skirt surface waviness, roughness, axial skirt profile, bulk elastic deformations and thermal distortion, lubrication and friction, and improving the numerical procedure for better computational efficiency. Parameters such as piston skirt profile, piston to liner clearance, surface roughness, and oil availability are examined for design purposes.

An original multi-body dynamics simulation program for reciprocating engine system with elastically deformable piston skirt was developed by Kimura et al. [11] in order to examine the secondary motion of piston. The program uses specialized equations of motion using only the rotational degree of freedom of each component taking the variation of rotating speed of crank into account. A general code solving the equations of motion for any number of cylinders was generated. Friction calculations were done simply using the Stribeck diagram.

Based on their previous studies, Etsion and Gommed [12] optimized the design of a non-cylindrical, gas-lubricated, ringless piston. In the solution for pressure distribution, they used the dimensionless form of Reynolds equation without flow factors. For the optimization, they considered piston stability and gas leakage, and presented some profiles with improved characteristics. Prata et al. [13] also studied on ringless pistons for small reciprocating compressors. They developed a simple model for oil-lubricated pistons, using average Reynolds equation without considering surface roughness effects on lubricant flow. Piston and liner were taken as rigid and between them hydrodynamic lubrication was assumed. Using a transparent test setup, this assumption had been observed to be valid for almost entire engine cycle.

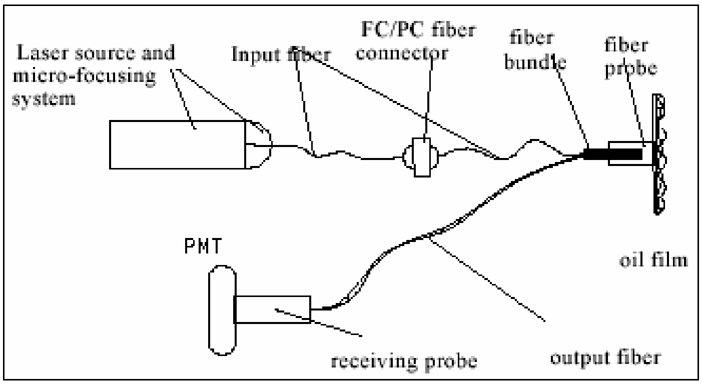

Figure 1.4 : Schematic drawing of oil film thickness measuring equipment [14]

Yang et al. [14] constructed a detailed model for secondary motion of the piston taking hydrodynamic lubrication, asperity contact and surface roughness effects on lubricant flow into account. Elastic deformations are considered in asperity contact condition only. Broyden method was used in the numerical solution, which was found out to have more tendency to converge than any other previously-used methods did. They also ran tests to validate their model. Laser induced fluorescent method was adopted in the equipment and the system included laser source and micro-focusing system, input fiber, FC/PC fiber connector, fiber bundle, output fiber, fiber probe, and receiving probe as shown in Figure 1.4 and Figure 1.5.

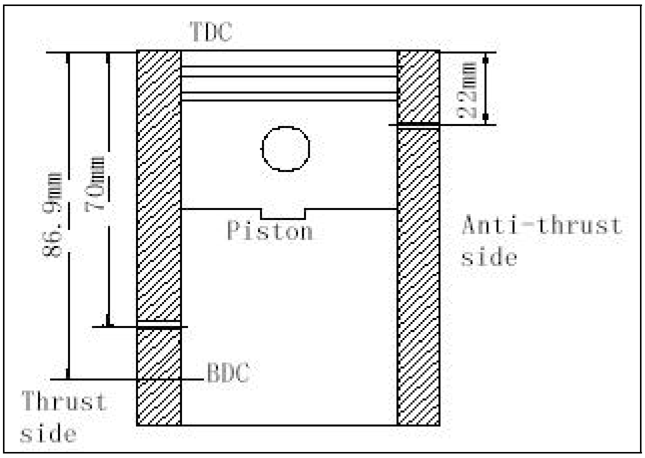

Figure 1.5 : Position of the fiber probe [14]

A simple algorithm was developed by Scholz and Bargende [15] for hydrodynamic contact lubrication. Roughness contact pressure was calculated and cavitation was included in the model. Secondary dynamics was not analyzed but this model is coupled to a FE model to solve for a piston-liner assembly. Results were than compared to those of a previously-run test. However, they were not found in good agreement with each other.

Duyar et al. [16] improved the model of Dursunkaya et al. [8] by incorporating the partially-flooded lubrication case and cavitation analysis. To deal with the extent of lubrication, the mass conserving Reynolds equation solver of journal bearing analysis code, ORBIT, was adopted for skirt-liner lubrication. A variable called a nodal switch was used in the equations to distinguish between the flooded and cavitated nodes. Mass fluxes in the two-dimensional mass conserving Reynolds equation were expressed in terms of these nodal switches in the discretized form. In addition to allowing for the specification of an oil supply, the cavitation region is more accurately represented since the appropriate Reynolds boundary condition for oil film detachment and the Jakobsson-Floberg-Olsson (JFO) boundary condition for subsequent film re-attachment are applied.

1.3.2 Studies on Piston Ring Lubrication

Beside skirt lubrication analysis, studies on piston ring-liner pair have been carried out in order to determine lubrication characteristics and dynamic behavior of rings.

Chung et al. [17] analyzed fire ring wear. They solved Reynolds equation for uni-directional flow without roughness effects. They calculated hydrodynamic friction force from pressure distribution and took the boundary lubrication friction coefficient from the Stribeck diagram. For the mixed lubrication case, they used both hydrodynamic and boundary lubrication friction coefficients with a multiplier expressing the extent of metal-to-metal contact. Piston secondary motion and cavitation were not taken into account.

Jun et al. [18] used a contact factor and simplified the average Reynolds equation to save computational time. They assumed uni-directional lubricant flow and used Greenwood and Tripp's [2] asperity contact approach.

Yu et al. [19] gave an analytical solution of piston ring pack lubrication. They used full mass conservation boundary conditions theory defined by JFO to model cavitation. They also presented the details of open and enclosed cavitation patterns. JFO boundary condition was applied at the points of reformation of the oil film in enclosed cavitation.

Stanley et al. [20] constructed a simplified friction model for piston-ring assembly. They generated Stribeck curves using Reynolds equation for different ring profiles and used them in the calculation of the ring friction. They also model the skirt friction with two-dimensional Reynolds equation. In ring friction, effects of surface characteristics, such as geometry and roughness, were included by means of a coefficient in the equation. In skirt lubrication part, surface roughness was neglected.

Zhang et al. [21] performed a two-dimensional piston ring lubrication analysis. They included flow factors of Patir and Cheng [3,4], asperity contact model of Greenwood and Tripp [2], Roeland's equation for viscosity-temperature-pressure effects, lubricant temperature variation and cylinder liner deformations.

Akalin and Newaz [22] solved uni-directional Reynolds equation as in the model of Yun et al. [18] and included cavitation algorithm. They used Reynolds (Swift-

Stieber) boundary conditions at film rupture locations. Surface roughness and asperity contact were considered. Contact load was calculated using Greenwood and Tripp's [2] model. In the second part of their study, Akalin and Newaz [23] correlated the results of their model with data from a bench test system developed by Akalin and Newaz [24].

Priest et al. [25] studied on cavitation in piston rings. They make a detailed review of different boundary conditions defined in the literature for film rupture and reformation. In their model, they applied these conditions and compared the results.

1.3.3 Experimental Analysis of Piston Secondary Dynamics

Test runs have been performed by several researchers to get experimental data and validate simulation results.

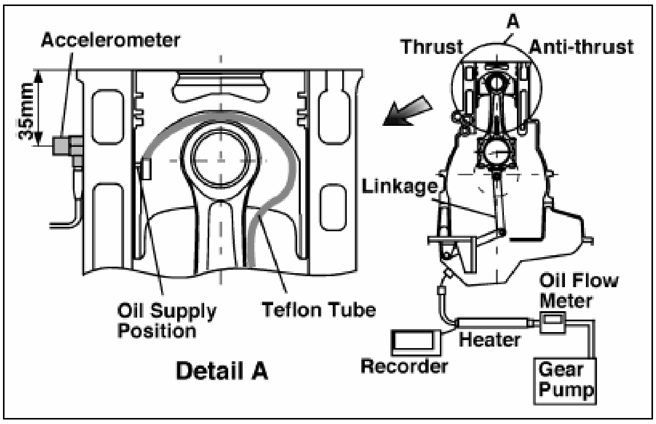

Figure 1.6 : Oil supply system used in the experiments held by Teraguchi et al. [26]

Teraguchi et al. [26] made experiments on the effects of oil supply on the cylinder block vibration, piston friction force, slap motion and oil consumption. Tests were run on a 1.7 liter, four-cylinder diesel engine varying the position of oil supply as shown in Figure 1.6 and Figure 1.7.

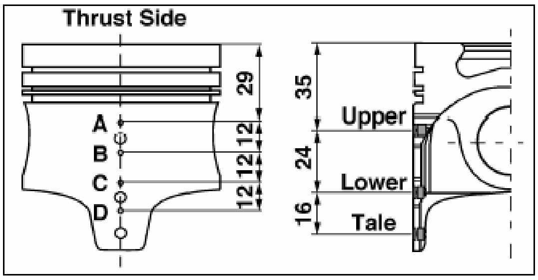

Figure 1.7 : Measuring points of piston motion [26]

Friction losses for pistons with different surface roughness and finish methods were investigated by Sato et al. [27]. A single-cylinder diesel engine was adapted to the floating liner method as shown in Figure 1.8 and friction force during the engine cycle was measured. Surface treatment methods such as plateau honing, etching and DLC coating were tested and comparisons were presented.

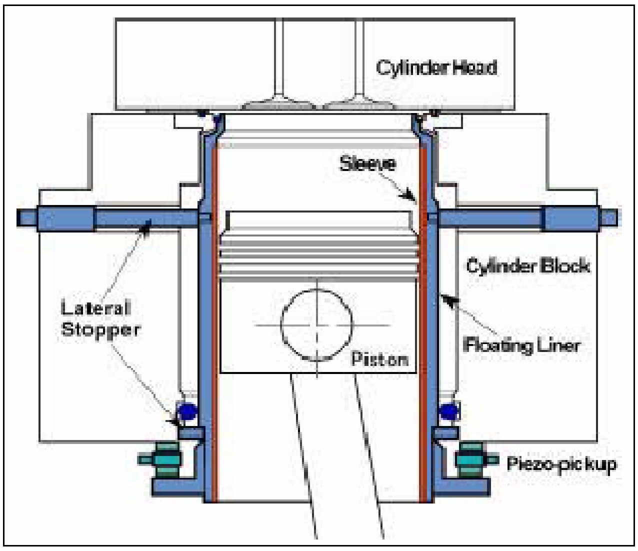

Figure 1.8 : Floating liner device modified into sleeve type [27]

Shin et al. [28] tried to validate previous numerical studies for the effect of offset crankshaft on friction performance of an internal combustion engine. A 4.2-liter I6 engine with an offset of 18 mm. (Figure 1.3) was constructed and measurements were compared to those obtained from the baseline version of the same engine.

Dellis and Arcoumanis [29] ran experiments on a reciprocating test rig to visualize cavitation between a piston ring and liner throughout the stroke using a charge-coupled device (CCD) camera. Different cavitation patterns such as fern, fissure, string cavities and bubbles were observed and discussed.

1.4 Objectives

The primary objective of this study is to determine the contribution of piston skirt lubrication to total assembly friction.

In addition to this, it is aimed to develop a tool to optimize friction, wear and lubrication properties of power cylinder components.

As the final objective, piston skirt lubrication characteristics including cavitation, surface texture, skirt profile and material properties will be analyzed using a two-dimensional flow model.

2 THEORY

2.1 Lubrication Theory

2.1.1 Lubrication Regimes

In the case of contact of two sliding rough surfaces, three different behaviors of the lubricant are observed. These are:

- Boundary lubrication
- Mixed lubrication
- Hydrodynamic lubrication
  - Elastohydrodynamic lubrication

In hydrodynamic lubrication regime, a full fluid film forms between the surfaces and the surfaces are completely separated. The most important property is dynamic viscosity of the lubricant. Elastohydrodynamic lubrication is similar to hydrodynamic lubrication in the context of surface separation, but as a result of relatively high normal load to be carried by the contact or relatively small clearance, the effect of elastic deformations is more significant. In addition, pressure dependence of viscosity also gets important in this regime. Likely, in the case of thermally transient applications, effects of thermal deformations and temperature dependence of viscosity should also be taken into consideration.

A contact in boundary lubrication regime behaves almost like a dry contact. Since the surfaces are too close to each other, a full fluid film cannot form within the spaces between asperities. The effect of lubricant stays at the level of chemical actions of thin films of molecular proportions.

In mixed lubrication regime, there is asperity contact to some extent. Fluid film forms in available spaces but is continuously deformed by asperities passing through. Characteristics of both hydrodynamic and boundary lubrication are observed.

In the literature, starved, partial and fully-flooded lubrication terms are also used for boundary, mixed and hydrodynamic lubrication, respectively. Patir and Cheng defines $H_\sigma = 3$ as the point of transition from mixed to hydrodynamic regime and names the lubrication of contacts with $H_\sigma < 3$ as partial lubrication.

In Figure 2.1, effect of lubrication regimes on friction can be seen. The diagram was drawn in the light of Richard Stribeck's experiments on plain journal bearing friction, the results of which were subsequently reordered by Ludwig Gumbel. Stribeck diagram shows the variation of friction coefficient with Sommerfeld grouping, $(\eta N/P)$, where η is dynamic viscosity, N is the rotational speed for a journal bearing (or sliding velocity, in general) and P is specific pressure (or normal load, in general). To make the behavior of the surfaces clear, film thickness ratio (H_σ), which is defined as the ratio of effective film thickness to surface roughness, can be used on the abscissa [1]. As the surfaces get apart from each other, the number of asperity peaks high enough to interact with those of the other surface decreases and the regime tends to be more hydrodynamic.

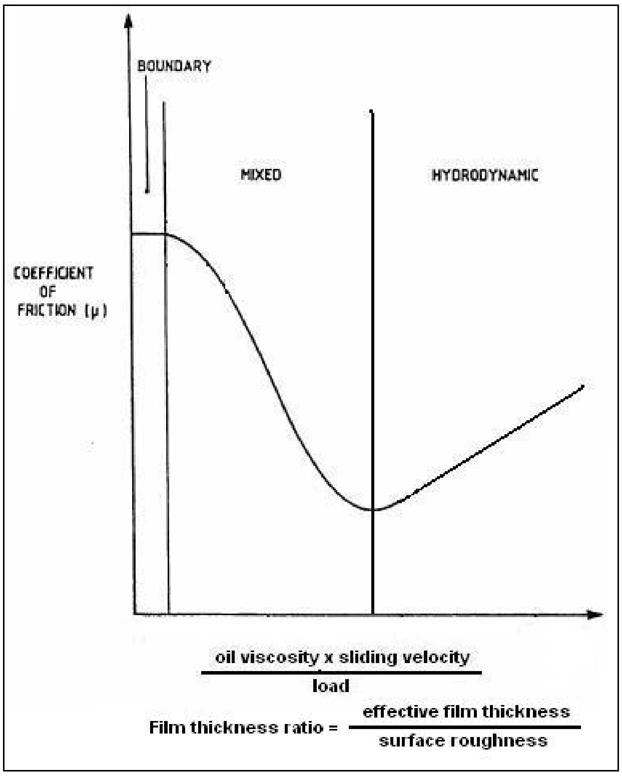

Figure 2.1 : Stribeck diagram

Friction coefficient remains approximately constant in boundary lubrication regime. It is not affected by the change in lubricant viscosity, relative velocity or normal contact load. From the film thickness ratio point of view, up to a certain value of film thickness, friction coefficient does not vary. With a further increase in film thickness, fluid film starts to build up and become effective in load carrying. At the point of transition to mixed lubrication regime, friction coefficient starts decreasing, as expected. It decreases until the asperity contact gets insignificant or ceases completely, and the regime turns to hydrodynamic lubrication. Therefore, for a steady-state EHD contact application, operation in the transition region from mixed to hydrodynamic lubrication should be aimed in order to minimize friction loss. To prevent solid-to-solid contact and reduce wear, Sommerfeld group may be shifted slightly towards hydrodynamic region. In practice, at a steady-state application, after some time of operation in the transition region, high peaks will be worn first and hydrodynamic lubrication will be reached.

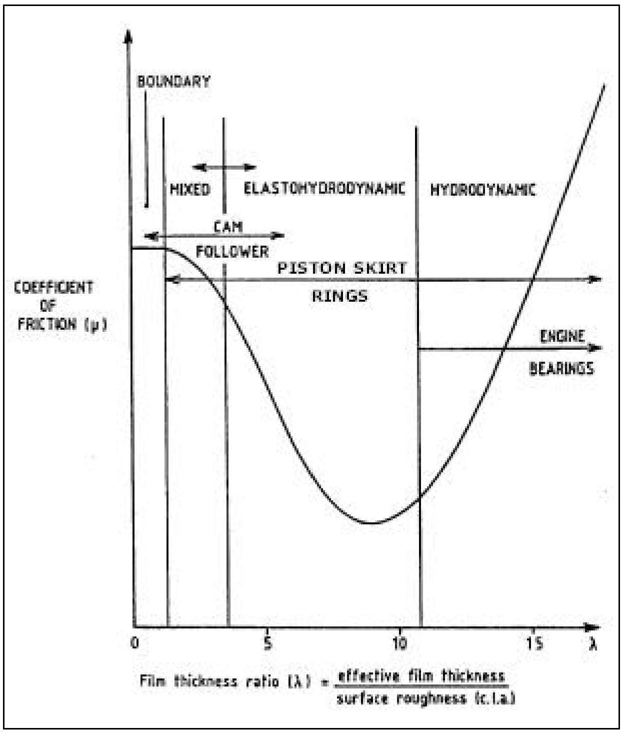

Figure 2.2 : Stribeck diagram showing the lubrication regimes for lubricated parts of an automobile engine [1]

However, in the case of ICE or compressor piston assembly lubrication, steady-state operation is impossible because of the variable forces acting on the piston during a complete power cycle, even at constant speed and load conditions. Figure 2.2 shows lubrication characteristics in an automobile engine piston assembly, together with some other lubricated parts of the engine. Piston ring and skirt lubrication falls in a wide range that spans mixed and hydrodynamic lubrication regions.

2.1.2 Inlet and Outlet Conditions of Lubricant Film

2.1.2.1 Effect of oil supply at the inlet

Amount of lubricant supplied to the EHD contact has great importance on the quality of lubrication. First of all, the sliding surface in the hydrodynamic contact requires enough amount of oil present at its leading edge in order to form a film layer. As this amount decreases, the lubrication regime shifts towards boundary lubrication.

The amount of oil supply may be represented with the thickness of oil on the cylinder liner at the leading edge side. As a result of the geometry of the convergent section of barrel profile, inlet location shifts towards the leading edge side and effective lubrication length increase as the supply oil film thickness increases. This can be seen in Figure 2.3. For an ICE piston skirt, this thickness is set by the operation of oil ring while the piston is moving towards TDC, and by the amount left from the previous cycle of the piston and wetting mechanisms such as oil jet and splashing of crank while the piston is moving towards BDC. During movement of a ringless compressor piston towards TDC, oil supply is limited by only the remaining amount from the downstroke. Therefore, design of the oil supply mechanisms is quite important.

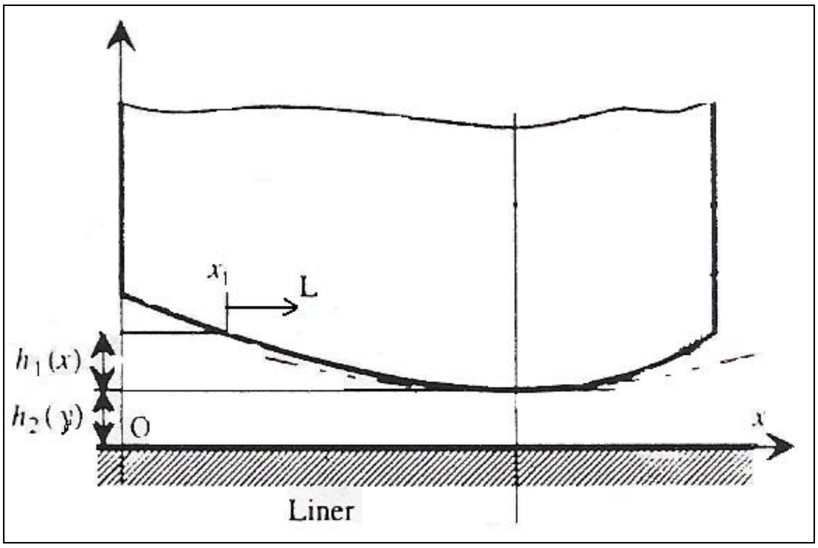

Figure 2.3 : Effect of supply oil thickness on effective lubricated length

Depending on the sufficiency of supply oil, inlet conditions can be named as:

- Fully-flooded inlet
- Partially-flooded inlet
- Starved inlet

and sufficiency can be decided comparing the existing oil thickness to the reference value predicted at design stage.

In most of the lubrication studies, fully-flooded inlet condition is assumed and a stationary inlet location is set. If the thickness of supply oil can be calculated, the exact inlet location can be found using the instantaneous orientation of the piston and geometric relations of barrel profile. Since the calculation of the supply oil thickness brings too much complexity to the problem, rough predictions may be more practical.

2.1.2.2 Outlet conditions and cavitation

Lubricant film loses its capacity to carry load at the outlet location and separates from the sliding surface. A good design is achieved when the outlet is located as close to the trailing edge as possible. This increases the effective lubrication length and provides a smoother operation to the piston. In piston skirt lubrication, the approach is to determine piston skirt length according to the possible outermost inlet and outlet locations. If a section at the leading or trailing edge is not wetted at all under any operating conditions, either the barrel profile can be flattened to make use of the whole skirt length or unwetted section can be cut out to reduce piston mass.

In transient lubrication conditions, especially in the case of skirt lubrication, it is difficult to predict a fixed outlet location due to cavitation. Cavitation term is used for the rupture of fluid film at locations where pressure drops under a certain value. This value may be the saturation pressure of air which is close to ambient pressure or the trailing edge pressure. Under no-cavitation conditions, this pressure drop to trailing edge pressure or -if the trailing edge pressure is the ambient pressure- to ambient pressure is expected to happen at the end of the effective lubrication length. Rupture before the outlet location takes place because of the incapability of the lubricant to have pressures below ambient or in other words to carry tensile load.

Reason for pressure drop is the increase in local film thickness due to:

- divergent section of the barrel profile
- negative squeeze film effect

In the case of piston skirt and ring lubrication, locations at which the fluid film ruptures in no-cavitation and cavitation conditions are shown in Figure 2.4. x_i, x_o and x_c are inlet, outlet and rupture locations, respectively, and p_L and p_T are leading and trailing edge pressures, respectively. L is the predicted effective lubrication length.

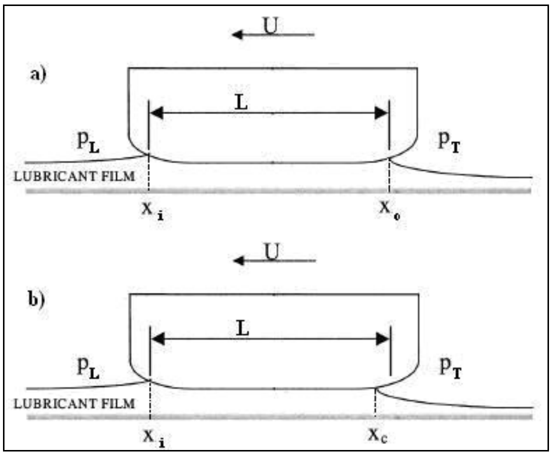

Figure 2.4 : Lubricated length on a piston skirt or ring surface in a) no-cavitation and b) cavitation conditions

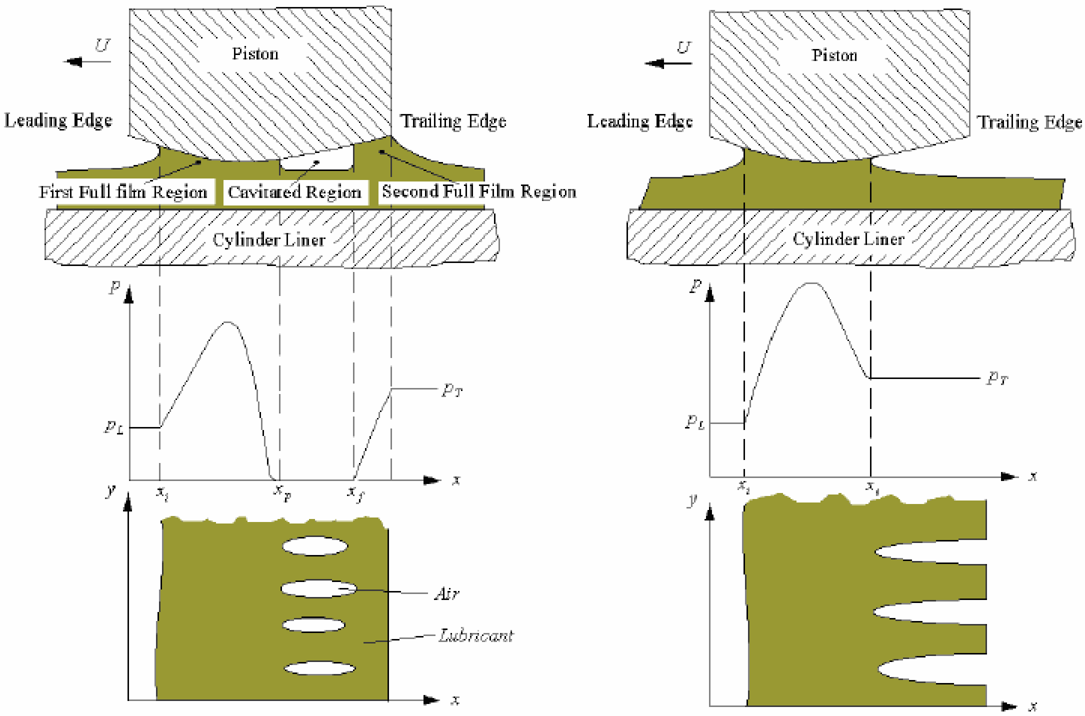

Figure 2.5 : a) Enclosed and b) open cavitation patterns [19]

Two types of cavitation, schematics of which are shown in Figure 2.5, have been defined in the literature:

- Enclosed cavitation
- Open cavitation

In enclosed cavitation, fluid film ruptures at x_p, a point somewhere in the divergent passage, and reforms at x_f since trailing edge pressure is higher than that in the cavitated region. Reason for cavitation is the drop of local pressure below the saturation pressure of air which is dissolved in the oil. According to JFO theory, pressure inside the cavitated zones is constant and close to ambient pressure.

In open cavitation case, film rupture occurs at x_p and cannot reform. In this case, the reason is oil starvation. Pressure at the cavitated zone is the trailing edge pressure. At the strips of lubricant between the cavitated zones, high pressure cannot develop. Although those areas are wetted, oil film cannot provide additional support to piston skirt. This behavior of lubricant film is also called flow separation in the literature.

In Figure 2.6-8, pressure distributions along the lubricant film according to some different approaches are shown [25]. In these figures, inlet, film rupture, film reformation and outlet locations are denoted by x_1, x_2, x_3 and x_4, respectively.

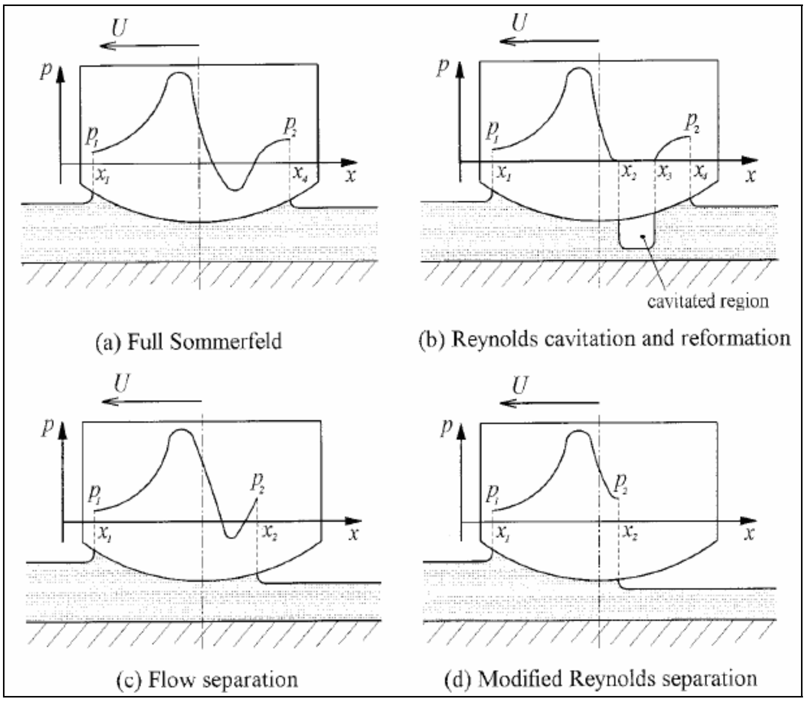

Figure 2.6 : Pressure distribution along fluid film according to a) Full Sommerfeld, b) Reynolds cavitation, c) flow separation and d) Reynolds separation approaches [25]

The simplest approach was suggested by Sommerfeld in 1904 [25]. Outlet pressure was set to trailing edge pressure:

$$at \ \ x = x_1 , \qquad p = p_L \tag{2.1}$$

$$at \ \ x = x_4 , \qquad p = p_T \tag{2.2}$$

These boundary conditions lead to large negative pressures in the divergent passage, Figure 2.6-a. In 1921, Gümbel recognized the inability of oil film to sustain negative pressures and simply set the negative pressures to ambient pressure or zero gauge, practically creating a cavitated region [25]. These conditions are referred to as the Gümbel or Half-Sommerfeld boundary conditions (Figure 2.7) [25]. However, this approach violates the mass continuity in the flow field.

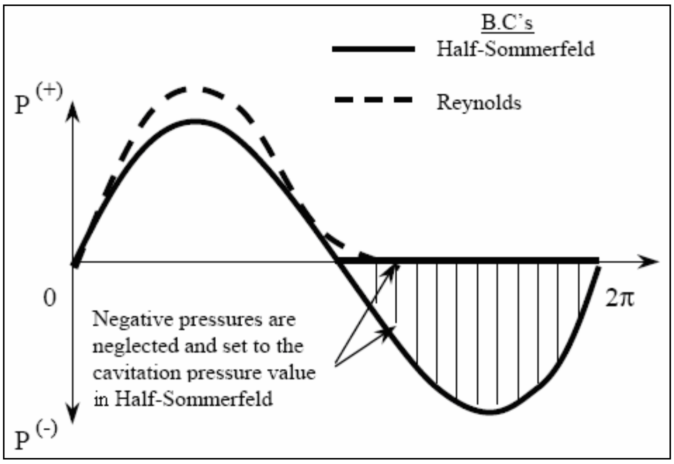

Figure 2.7 : Pressure distribution along fluid film according to Half-Sommerfeld cavitation and Reynolds flow separation approaches

Reynolds appreciated the role of cavitation in his classical work on lubrication theory, leading later to the formulation of the Reynolds cavitation condition independently by Swift and Steiber:

$$at \ \ x = x_1 , \qquad p = p_L \tag{2.3}$$

$$at \ \ x = x_2 , \qquad p = p_T \ , \ \ \frac{\partial p}{\partial x} = 0 \tag{2.4}$$

which is superior to Half-Sommerfeld boundary conditions since it correctly accounts for oil flow continuity across the cavitation boundary [25]. Film reformation condition was then formulated by Dawson et al. again from the oil flow continuity [25]:

$$at\ \ x = x_3\ , \qquad p = 0\ ,\ \frac{\partial p}{\partial x} = 6\ \mu\ U \left(\frac{h_2 - h_3}{h_3^{\ 3}} \right) \tag{2.5}$$

An alternative approach belongs to Dawson and Taylor, proposing that flow separation occurs rather than cavitation [25]. The simplest flow separation model is referred to as full-fluid-film condition leading to the formulation derived from Navier-Stokes equations:

$$at\ \ x = x_2\ , \qquad p = p_T\ ,\ \frac{\partial p}{\partial x} = \frac{2\ \mu\ U}{h_2^{\ 2}} \tag{2.6}$$

The full-fluid-film condition is approximate, however, since a full fluid film is assumed and no development of the lubricant-gas interface is considered. This deficiency was overcome by Coyne and Elrod [31-32] who defined the boundary conditions as:

$$at\ \ x = x_3\ , \qquad p = 0\ ,\ \frac{\partial p}{\partial x} = \frac{6\ \mu\ U}{h_2^{\ 2}} \left(1 - 2\ \frac{h_\infty}{h_2} \right) \tag{2.7}$$

In flow separation approach, the hydrodynamic pressure profile is characterized most significantly by a small subambient pressure loop upstream of the point of separation as shown in Figure 2.6c.

Wakuri et al. proposed that the lubricant cavitates with no reformation [25]. The justification for this proposal was the equality of saturation pressure of the gas to trailing edge pressure. Richardson and Borman, and Taylor et al. applied these boundary conditions but treated the rupture as flow separation rather than cavitation based on their experimental observations [25]. This case (Figure 2.6c) is referred to as modified Reynolds separation with the boundary conditions being the same as Reynolds cavitation:

$$at \;\; x = x_2 \; , \qquad p = p_T \; , \;\; \frac{\partial p}{\partial x} = 0 \tag{2.8}$$

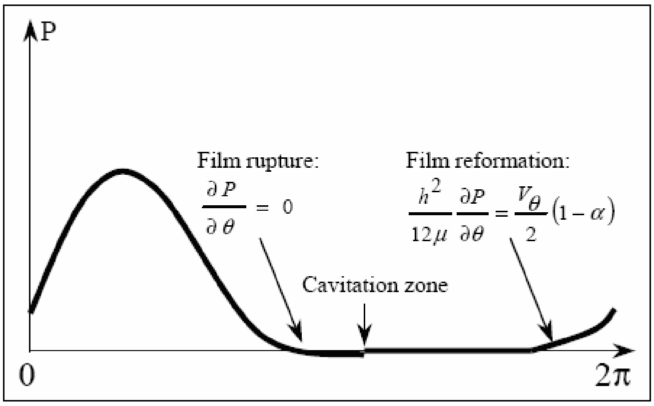

Figure 2.8 : Pressure distribution and boundary conditions with Reynolds cavitation and JFO film reformation

The last approach that will be mentioned here is the JFO (Jakobsson-Floberg-Olsson) reformation conditions. After rupturing according to the Reynolds pressure gradient condition, lubricant film reforms satisfying the formulation shown in Figure 2.8.

2.2 Governing Equations

2.2.1 Equations of Motion

For the solution of lateral motion of the piston, equations of motion for both piston and connecting rod are written using the coordinate system shown in Figure 2.9.

Forces acting on the piston are gas force, pin force due to the reaction from connecting rod, normal force on piston skirt surface due to lubricant pressure and contact, friction due to viscous effect of lubricant and solid-to-solid contact. Moments on the piston are pin moment due to friction, moments resulting from normal and tangential forces on the piston. These forces and moments are named in Figure 2.10.

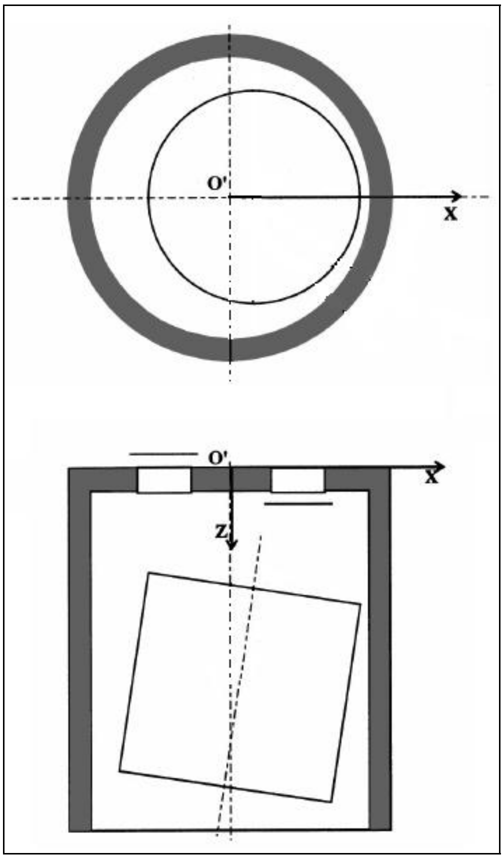

Figure 2.9 : 2-D coordinate system fixed to the cylinder block

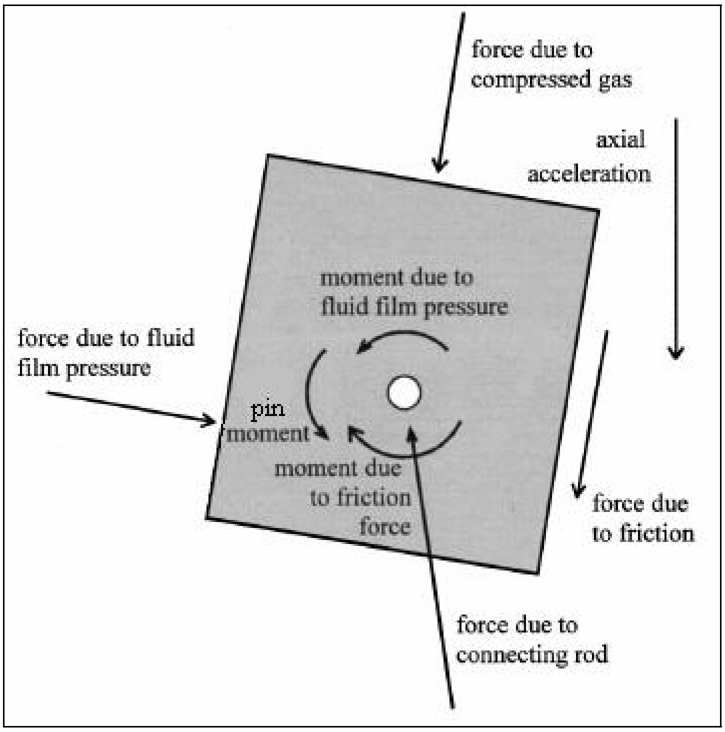

Figure 2.10 : Forces and moments acting on the piston

Forces and moments on the piston and connecting rod, and basic dimensions that are used in the calculations are shown in Figure 2.11 and Figure 2.12 respectively.

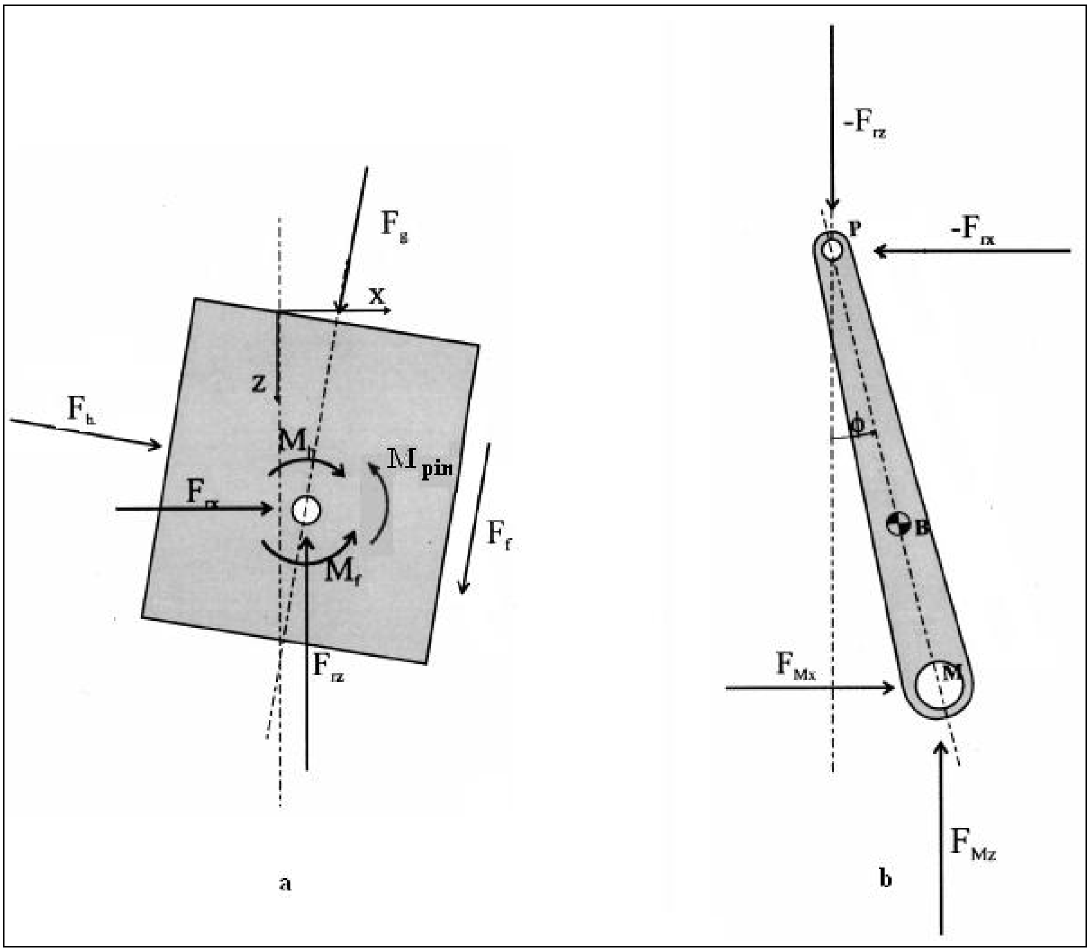

Figure 2.11 : Free-body diagrams of (a) piston and (b) connecting rod

Using these free-body diagrams, equations of motion for piston are written as:

$$F_g \sin\alpha + F_{rX} + F_h \cos\alpha + F_f \sin\alpha = m_p a_{pX} \tag{2.9a}$$

$$F_g \cos\alpha + F_{rZ} + F_h \sin\alpha + F_f \cos\alpha = m_p a_{pZ} \tag{2.9b}$$

$$M_{pin} + M_h + M_f = I_p \ddot{\alpha} \tag{2.9c}$$

Making use of *sin* $\alpha = 0$ and *cos* $\alpha = 1$ for small α, and neglecting M_{pin}, Eq.s (2.9) reduces to:

$$F_{rX} + F_h = m_p a_{pX} \tag{2.10a}$$

$$F_{rZ} - F_g + F_f = m_p \, a_{pZ} \tag{2.10b}$$

$$M_h + M_f = I_p \, \ddot{\alpha} \tag{2.10c}$$

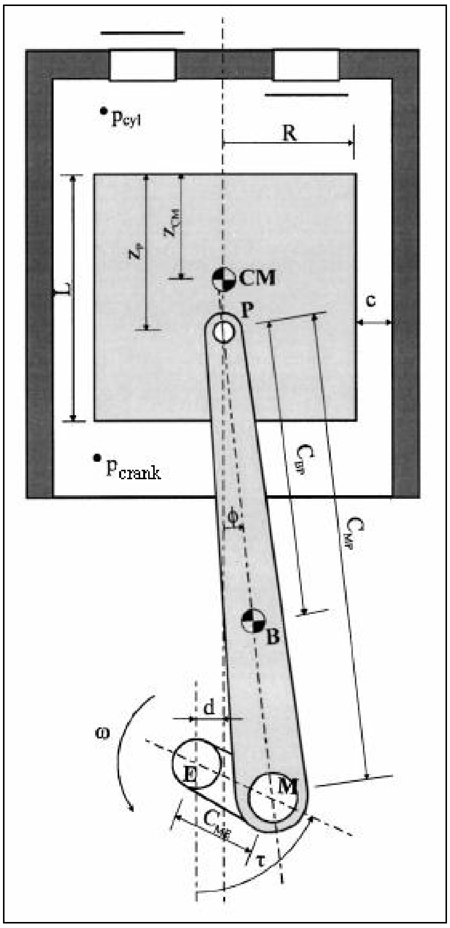

Figure 2.12 : Piston-cylinder system

Equations of motion for the connecting rod are:

$$F_{MX} - F_{rX} = m_b \, A_{bX} \tag{2.11a}$$

$$F_{MZ} - F_{rZ} = m_b \, A_{bZ} \tag{2.11b}$$

$$(F_{rZ} \, C_{BP} + F_{MZ} \, C_{MB}) \sin\phi - (F_{MX} \, C_{MB} + F_{rX} \, C_{BP}) \cos\phi = I_b \, \ddot{\phi} \tag{2.11c}$$

Arranging Eq.s (2.11) and Eq. (2.10b), F_{rX} is written as:

$$F_{rX} \;=\; \frac{\left[\left(m_p a_{pX} + F_g - F_f\right) C_{MP} + m_b A_{bZ} C_{MB}\right] \sin\phi - m_b A_{bX} C_{MB} \cos\phi - I_b \ddot{\phi}}{C_{MP} \cos\phi} \tag{2.12}$$

Therefore, the set of equations to be solved becomes:

$$F_{rX} \;+\; F_h \;=\; m_p \; a_{pX} \tag{2.13a}$$

$$M_h \;+\; M_f \;=\; I_p \; \ddot{\alpha} \tag{2.13b}$$

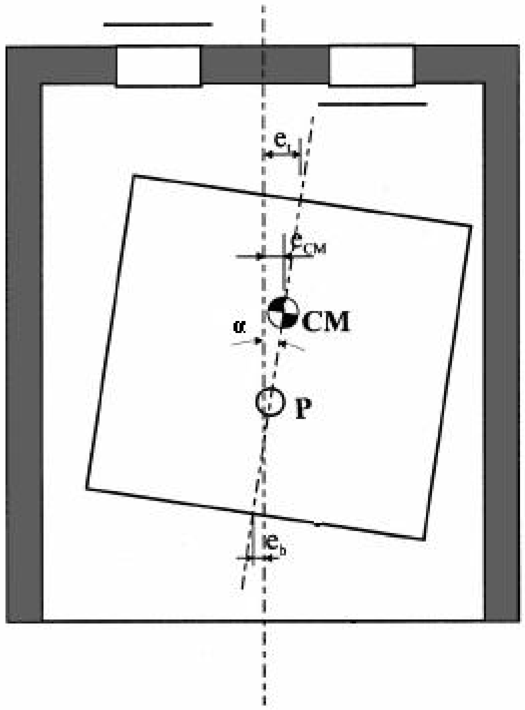

Figure 2.13 : Lateral displacement of piston

The lateral motion of the piston in X-direction can be defined in terms of displacements and tilt angle shown in Figure 2.13. e_t, e_b and e_{CM} stand for displacements of piston top, bottom and mass center, respectively, form cylinder axis, and α stands for the tilt angle with respect to cylinder axis. Any two of these four parameters can be used to define the instantaneous position of the piston relative to the cylinder block, and they can be written in terms of each other by means of the following relations:

$$e_{CM} = e_t - \frac{z_{CM}}{L}\left(e_t - e_b\right) \tag{2.14a}$$

$$\alpha = \frac{\left(e_t - e_b\right)}{L} \tag{2.14b}$$

In this study, piston top and bottom eccentricities were chosen to represent the lateral motion of the piston inside the cylinder for simplicity in further calculation of the local film thickness values around the piston skirt.

Lateral and angular accelerations of the piston are found as:

$$\ddot{e}_{CM} = \ddot{e}_t - \frac{z_{CM}}{L}\left(\ddot{e}_t - \ddot{e}_b\right) \tag{2.15a}$$

$$\ddot{\alpha} = \frac{\left(\ddot{e}_t - \ddot{e}_b\right)}{L} \tag{2.15b}$$

Letting $a_{pX} = \ddot{e}_{CM}$ and substituting Eq.s (2.15) into Eq.s (2.13), the coupled equations of motion can be written in terms of piston top and bottom accelerations.

$$F_{rX} + F_h = m_p\left[\left(1 - \frac{z_{CM}}{L}\right)\ddot{e}_t + \frac{z_{CM}}{L}\ddot{e}_b\right] \tag{2.16a}$$

$$M_h + M_f = I_p\left(\frac{\ddot{e}_t - \ddot{e}_b}{L}\right) \tag{2.16b}$$

Finally, the problem reduces to the coupled solution of two equations with two unknowns which can be written in matrix form as follows:

$$\begin{bmatrix} m_p\left(1-\dfrac{Z_{CM}}{L}\right) & m_p\dfrac{Z_{CM}}{L} \\ \dfrac{I_p}{L} & -\dfrac{I_p}{L} \end{bmatrix}\begin{bmatrix} \ddot{e}_t \\ \ddot{e}_b \end{bmatrix} = \begin{bmatrix} F_{rx} + F_h \\ M_h + M_f \end{bmatrix} \tag{2.17}$$

In order to solve Eq. (2.17), normal and tangential forces, F_h and F_f, respectively, and their moments about the pin axis, M_h and M_f have to be determined.

In hydrodynamic lubrication regime, only the hydrodynamic pressure of oil film supports the piston in the lateral direction. In the axial direction, only viscous shearing force acts on the piston skirt causing viscous friction. In this regime, normal force can be calculated by simply integrating the pressure over the skirt surface and friction force can be found by integrating viscous shearing pressure and asperity side pressure for rough surfaces.

In mixed lubrication regime, in addition to the hydrodynamic pressure, solid-to-solid contact force develops as a result of asperity contact. In this regime dry friction should also be added to viscous friction taking the extent of asperity contact into account.

2.2.2 Reynolds Equation

For an isothermal, incompressible lubricant, the pressure in elastohydrodynamic contacts is governed by Reynolds equation:

$$\frac{\partial}{\partial x}\left(\frac{h_T{}^3}{12\mu}\frac{\partial p}{\partial x}\right) + \frac{\partial}{\partial y}\left(\frac{h_T{}^3}{12\mu}\frac{\partial p}{\partial y}\right) = \frac{U_1 + U_2}{2}\frac{\partial h_T}{\partial x} + \frac{\partial h_T}{\partial t} \tag{2.18}$$

with x being the sliding direction. h_T is mean local thickness, and U_1 and U_2 are absolute velocities of sliding surfaces.

In Eq. (2.18), the two terms on the LHS are the mass transport in x and y-directions, respectively, due to pressure gradient. The first term on the RHS is the mass transport due to change in the film thickness along the direction of the lubricant flow and the last term is the squeeze film velocity. Squeeze film effect is the change in film thickness due to the movement of the surfaces towards or away from each other.

Reynolds equation was modified by Patir and Cheng [3] in order to include surface roughness effects. Modified Reynolds equation for a two-dimensional flow can be expressed as:

$$\frac{\partial}{\partial x}\left(\phi_x \frac{h^3}{12\mu}\frac{\partial \overline{p}}{\partial x}\right)+\frac{\partial}{\partial y}\left(\phi_y \frac{h^3}{12\mu}\frac{\partial \overline{p}}{\partial y}\right) = \frac{U_1+U_2}{2}\frac{\partial \overline{h}_T}{\partial x}+\frac{U_1-U_2}{2}\sigma\frac{\partial \phi_s}{\partial x}+\frac{\partial \overline{h}_T}{\partial t} \tag{2.19}$$

In the modified form, two pressure flow factors, ϕ_x and ϕ_y, and a shear flow factor ϕ_s are incorporated into the average Reynolds equation. Pressure flow factors compare the average pressure flow on a rough surface to that of a smooth one. Shear flow factor represents the additional flow due to sliding in a rough bearing. In the case of piston skirt-cylinder bore interaction, one of the surfaces, cylinder wall, is stationary, $U_1 = U$ and $U_2 = 0$. Hence, Eq. (2.19) takes the following form:

$$\frac{\partial}{\partial x}\left(\phi_x\, h^3\, \frac{\partial \overline{p}}{\partial x}\right)+\frac{\partial}{\partial y}\left(\phi_y\, h^3\, \frac{\partial \overline{p}}{\partial y}\right) = 6\,\mu\, U\left(\frac{\partial \overline{h}_T}{\partial x}+\sigma\,\frac{\partial \phi_s}{\partial x}\right)+12\,\mu\,\frac{\partial \overline{h}_T}{\partial t} \tag{2.20}$$

2.2.3 Flow Factors

Flow factors are strongly dependent on roughness of both surfaces and directional properties of the asperities. Flow factors were defined by Patir and Cheng [4] as functions of H_σ and γ.

$$\phi_x = \phi_x(H_\sigma,\gamma) \tag{2.21}$$

$$\phi_y = \phi_y(H_\sigma,\gamma) \tag{2.22}$$

$$\phi_s = \phi_s(H_\sigma,\gamma) \tag{2.23}$$

where $H_\sigma = h/\sigma$ and γ is a characteristic of a surface expressing the orientation of the asperities with respect to the flow direction. It was defined as:

$$\gamma = \frac{\lambda_{0.5x}}{\lambda_{0.5y}} \tag{2.24}$$

where $\lambda_{0.5x}$ and $\lambda_{0.5y}$ are the lengths at which auto-correlation of a profile reduces to 50% of its initial value in the longitudinal (x) and transversal (y) directions, respectively. Schematics of surfaces with different orientation factor values are given in Figure 2.14. These three surfaces may have equal surface roughness values but their resistance or contribution to the flow differs significantly.

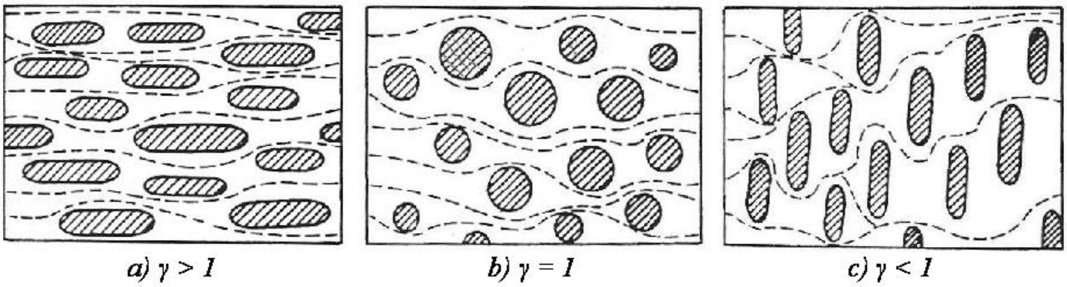

Figure 2.14 : Typical contact areas for a) longitudinally oriented, b) isotropic and c) transversely oriented surfaces [3]

Pressure flow factor is shown in Figure 2.15. It can be calculated using Eq. (2.25) with the coefficients given in Table 2.1**.**

$$\phi_x = \begin{cases} 1 - C\, e^{-r H_\sigma} & \gamma \le 1 \\ 1 + C\, H_\sigma^{-r} & \gamma > 1 \end{cases} \tag{2.25}$$

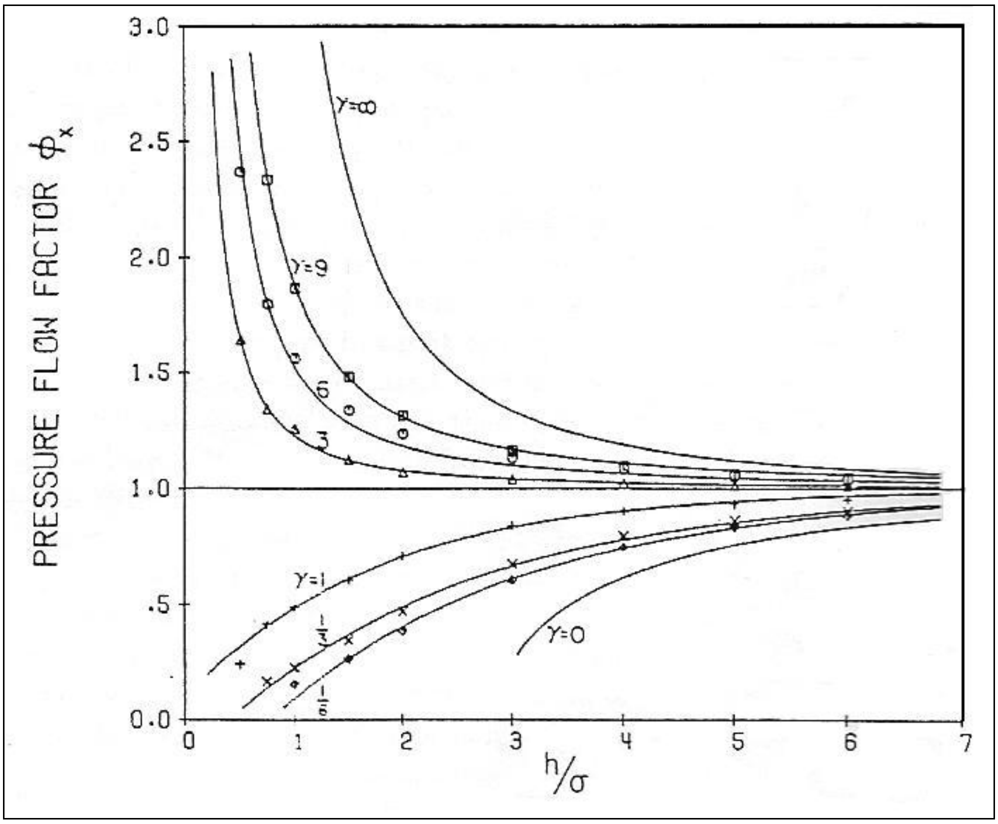

Figure 2.15 : Pressure flow factor [4]

Table 2.1 : Coefficients of Eq. (2.25) for ϕ_x [4]

γ	C	r	Range
1/9	1.48	0.42	$H_\sigma > 1$
1/6	1.38	0.42	$H_\sigma > 1$
1/3	1.18	0.42	$H_\sigma > 0.75$
1	0.90	0.56	$H_\sigma > 0.5$
3	0.225	1.5	$H_\sigma > 0.5$
6	0.520	1.5	$H_\sigma > 0.5$
9	0.870	1.5	$H_\sigma > 0.5$

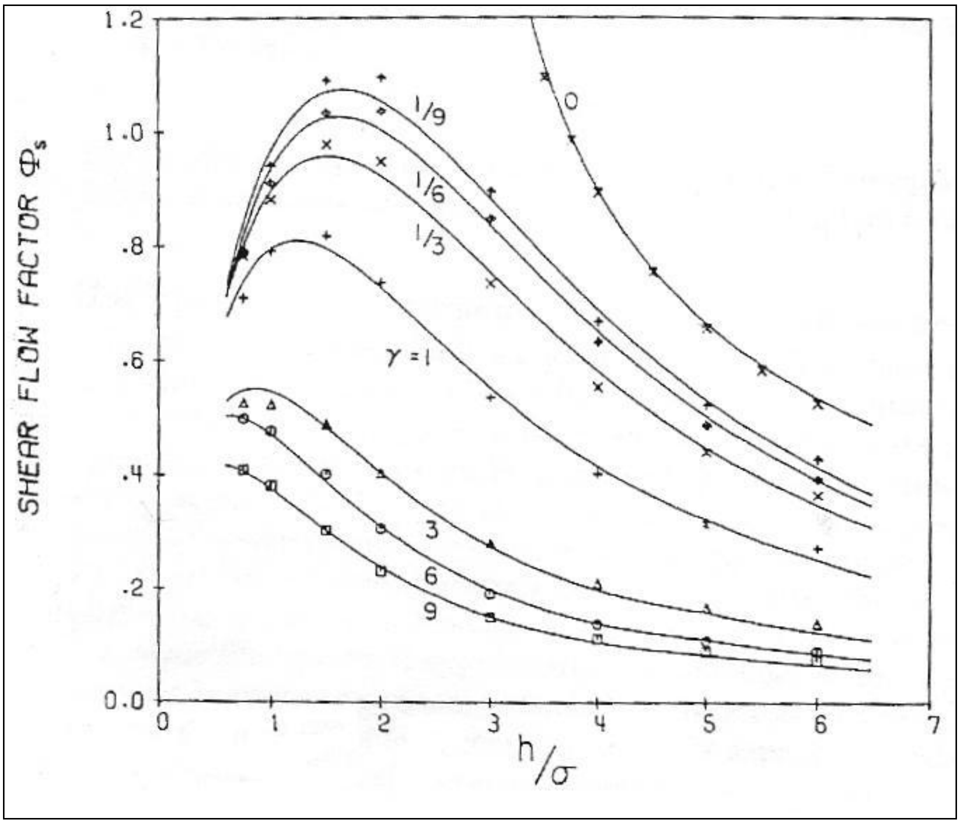

Figure 2.16 : Shear flow factor [4]

Table 2.2 : Coefficients of Eq. (2.29) for Φ_s for the range $H_\sigma > 0.5$ [4]

γ	A_1	α_1	α_2	α_3	A_2
1/9	2.046	1.12	0.78	0.03	1.856
1/6	1.962	1.08	0.77	0.03	1.754
1/3	1.858	1.01	0.76	0.03	1.561
1	1.899	0.98	0.92	0.05	1.126
3	1.560	0.85	1.13	0.08	0.556
6	1.290	0.62	1.09	0.08	0.388
9	1.011	0.54	1.07	0.08	0.295

One can easily note that ϕ_y can also be found using Table 2.1 such that:

$$\phi_y \left(H_\sigma,\gamma\right) = \phi_x \left(H_\sigma,\frac{1}{\gamma}\right) \tag{2.26}$$

Shear flow factor can be calculated by:

$$\phi_s = V_{r1}\ \Phi_s(H_\sigma,\gamma_1) - V_{r2}\ \Phi_s(H_\sigma,\gamma_2) \tag{2.27}$$

where

$$V_{r1} = \left(\frac{\sigma_1}{\sigma}\right)^2 \tag{2.28a}$$

$$V_{r2} = \left(\frac{\sigma_2}{\sigma}\right)^2 = 1 - V_{r2} \tag{2.28b}$$

and Φ_s is a parameter which is also called shear flow factor. However, one should keep in mind that Φ_s is associated with a single surface, while ϕ_s is for the combination of two surfaces brought together. Φ_s is shown in Figure 2.16 and it can be calculated using Eq. (2.29) whose coefficients are given in Table 2.2.

$$\Phi_s = \begin{cases} A_1\ H_\sigma^{\alpha_1}\ e^{-\alpha_2 H_\sigma + \alpha_3 H_\sigma^2} & H_\sigma \le 5 \\ A_2\ e^{-0.25 H_\sigma} & H_\sigma > 5 \end{cases} \tag{2.29}$$

2.2.4 Contact Load and Friction Forces

Solid-to-solid contact force can be calculated by the asperity contact model of Greenwood and Tripp [2] which was given as:

$$p_c = K\ E'\ F_{2.5}\left(H_\sigma\right) \tag{2.30}$$

where

$$K = \frac{16\sqrt{2}}{15} \pi \left(N \beta' \sigma\right) \sqrt{\frac{\sigma}{\beta'}} \tag{2.31}$$

and

$$E' = \frac{1}{\frac{1 - \upsilon_1^2}{E_1} + \frac{1 - \upsilon_2^2}{E_2}} \tag{2.32}$$

is the composite Young's modulus. In Eq. (2.31), N is the number of asperities per unit contact area and β' is the asperity radius of curvature. $F_{2.5}(H_\sigma)$ is the probability distribution of asperity heights. For the surface roughness with Gaussian distributed asperities, this formula is simplified by Hu et al. as follows:

$$F_{2.5}\left(H_\sigma\right) = \begin{cases} A\left(\Omega - H_\sigma\right)^Z & H_\sigma \le \Omega \\ 0 & H_\sigma > \Omega \end{cases} \tag{2.33}$$

where Ω = 4.0, A = 4.4068x10^{-5} and Z = 6.804. In Eq. (2.30), K is given as 1.198x10^{-4} by Hu et al.

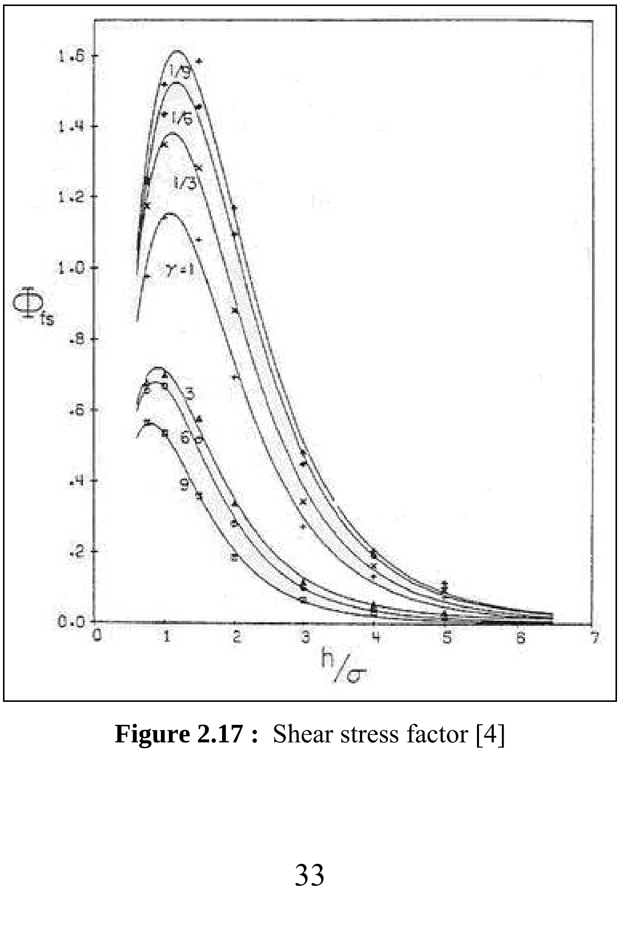

Figure 2.17 : Shear stress factor [4]

Table 2.3 : Coefficients of Eq. (2.36) for Φ_{fs} for the range $0.5 < H_\sigma < 7$ [4]

γ	A_3	α_4	α_5	α_6
1/9	14.1	2.45	2.30	0.10
1/6	13.4	2.42	2.30	0.10
1/3	12.3	2.32	2.30	0.10
1	11.1	2.31	2.38	0.11
3	9.8	2.25	2.80	0.18
6	10.1	2.25	2.90	0.18
9	8.7	2.15	2.97	0.18

For the contribution of solid-to-solid contact to skirt friction, asperity contact friction pressure can be calculated simply using the dry friction coefficient. Therefore, friction force on the piston skirt is governed by the following formula:

$$F_f = -sign(U) \int_A \left\{ \frac{\mu \, |U|}{h} \left[\left(\phi_f - \phi_{fs} \right) + 2 \, V_{r1} \, \phi_{fs} \right] + \mu_f \, p_c \right\} dA \qquad (2.34)$$

In Eq. (2.34), shear stress factor, ϕ_{fs}, is a correction term which arises from the combined effect of roughness and sliding, similar to the ϕ_s in the mean flow. The functional dependence of ϕ_{fs} on the roughness parameters is also similar to that of ϕ_s:

$$\phi_{fs} = V_{r1} \, \Phi_{fs}(H_\sigma, \gamma_1) - V_{r2} \, \Phi_{fs}(H_\sigma, \gamma_2) \qquad (2.35)$$

Φ_{fs} can be calculated using Eq. (2.36). Coefficients of the equation are presented in Table 2.3. The variation of Φ_{fs} with H_σ for different γ values is shown in Figure 2.17.

$$\Phi_{fs} = \begin{cases} A_3 \, H_\sigma^{\alpha_4} \, e^{-\alpha_5 H_\sigma + \alpha_6 H_\sigma^2} & 0.5 < H_\sigma \le 7 \\ 0 & H_\sigma > 7 \end{cases} \qquad (2.36)$$

ϕ_f is another correction factor that arises from averaging the sliding velocity component of the shear stress. Details, as well as the following formula written in a suitable form for efficient numerical calculation, can be found in Patir and Cheng [4].

$$\phi_f = \begin{cases} \dfrac{35}{32} z\left[\left(1-z^2\right)^3 \ln\dfrac{z+1}{\in *} + A\right] & H_\sigma \leq 3 \\ \dfrac{35}{32} z\left[\left(1-z^2\right)^3 \ln\dfrac{z+1}{z-1} + B\right] & H_\sigma > 3 \end{cases} \tag{2.37}$$

where

$$A = \frac{1}{60}\left[-55 + z\left(132 + z\left(345 + z\left(-160 + z\left(-405 + z\left(60 + 147z\right)\right)\right)\right)\right)\right] \tag{2.38}$$

$$B = \frac{z}{15}\left[66 + z^2\left(30z^2 - 80\right)\right] \tag{2.39}$$

$$z = \frac{H_\sigma}{3} \tag{2.40}$$

$$\in * = \frac{1}{300} \tag{2.41}$$

3 SOLUTION APPROACH

A MATLAB code was written in order to solve the secondary dynamics of a reciprocating piston with its skirt in mixed lubrication.

3.1 Assumptions and Simplifications

3.1.1 Elastic and Thermal Deformations

Elastic and thermal deformations of piston skirt and cylinder bore are neglected in this study. After warm up and under steady operating conditions, cylinder wall temperature does not vary significantly during a complete cycle. Temperature at piston crown, at the top-land over the first compression ring, and at the second-land between compression rings vary with time due to combustion, but piston skirt is relatively far from top regions and temperature can be taken as constant throughout a 720º CA cycle at constant load and speed. Therefore, thermal deformations can also be assumed constant and can be taken into account within the inputs for nominal clearance and barrel profile.

Unlikely, elastic deformations vary with time as a function of local pressures both on piston skirt-cylinder bore interaction and on piston pin and bearing area. This variation affects local film thickness values significantly. In some cases these deformations can reach the order of nominal clearance or deviations due to barrel profile. However, determination of elastic deformations necessitates a comprehensive submodel or a coupled operation of a FE model. In order to prevent the complexity it will bring to the solution, all the parts are assumed to be rigid.

3.1.2 Oil Supply

Partially-flooded inlet condition is applied assuming there is always a fluid film in front of the piston with a constant thickness of h_{max}. Piston surface touches the lubricant at the locations where the instantaneous gap is equal to h_{max} and pressure develops in the fluid film. Therefore, inlet location is set by this h_{max} value and it varies during the cycle depending on the instantaneous piston orientation at each crankangle.

3.1.3 Fluid and Flow Properties

Lubricant is assumed to be an incompressible, Newtonian fluid. Viscosity of the lubricant is independent of pressure and a function of only temperature. Since temperature is taken as constant, a single viscosity value can be used. For two different average contact temperatures which will be chosen as an input, two different oil viscosity data for SAE 5W/30 are available:

$$\text{for } \overline{T}_{contact} = 24^{\circ}C, \qquad \mu = 0.134\ Pa.s \tag{3.1}$$

$$\text{for } \overline{T}_{contact} = 70^{\circ}C, \qquad \mu = 0.023\ Pa.s \tag{3.2}$$

The flow is laminar.

3.1.4 Surface Properties

Surface of both skirt and cylinder were taken as rough surfaces, with asperities approximated by a Gaussian distribution. However, macroscale textures applied by coating, honing or laser surface texturing were not considered at this stage of the study.

3.1.5 Structural and Geometrical Simplifications

In the model, only skirt lubrication, and forces and moment acting on the piston through skirt section were taken into account. The two effects of rings were neglected; one is its contribution to piston friction and to balancing of especially tilting moment on the piston, and the other is the direct effect on skirt lubrication by determining the inlet oil supply thickness during piston's movement towards TDC. In addition, although the model is capable of dealing with noncylindrical piston geometry with slight modifications, the skirt was taken as a perfect cylindrical surface modified for the effect of barrel profile. Nevertheless, with its current form, the model is quite effective for oil-lubricated pistons of small reciprocating compressors, generally used in refrigeration applications.

3.2 Solution of Reynolds Equation for Hydrodynamic Pressure Distribution

As mentioned in Part 2.2.2, pressure distribution between two rough surfaces is governed by two-dimensional modified Reynolds equation. For the case in which one of the surfaces is stationary, Equation 2.20 will be solved using a finite differencing scheme.

Before applying finite differencing scheme, Eq. 2.20 is normalized by substituting the following non-dimensional parameters:

$$X = \frac{2x}{L} \tag{3.3}$$

$$Y = \frac{2y}{L} \tag{3.4}$$

$$H = \frac{h}{c} \tag{3.5}$$

$$T = t\,\omega \tag{3.6}$$

$$U^* = \frac{U}{r\,\omega} \tag{3.7}$$

$$P = \bar{p}\,\frac{c^2}{3\,\mu\,r\,\omega\,L} \tag{3.8}$$

$$\sigma^* = \frac{\sigma}{c} \tag{3.9}$$

$$\phi_c = \frac{\partial \bar{h}_T}{\partial h} \tag{3.10}$$

where ϕ_c is the contact factor defined by Wu and Zheng in order to approximate the average gap between the surfaces. ϕ_c is given as:

$$\phi_c = \frac{1}{2}\left[1 + erf\left(H_\sigma\right)\right] \tag{3.11}$$

where *erf* is the error function.

Thus, modified Reynolds equation takes the following non-dimensional form:

$$\frac{\partial}{\partial X}\left(\phi_x H^3 \frac{\partial P}{\partial X}\right)+\frac{\partial}{\partial Y}\left(\phi_y H^3 \frac{\partial P}{\partial Y}\right)=U*\left(\phi_c \frac{\partial H}{\partial X}+\sigma*\frac{\partial \phi_s}{\partial X}\right)+\beta\phi_c \frac{\partial H}{\partial T} \tag{3.12}$$

where $\beta = L/r$ is the squeeze film factor.

ϕ_x, ϕ_y, ϕ_s, H^3 and P are all implicit functions of X and Y, therefore they will be differentiated numerically. Substituting the following parameters:

$$C = \phi_x H^3 \tag{3.13}$$

$$D = \phi_y H^3 \tag{3.14}$$

and writing Eq. (3.12) again:

$$\frac{\partial C}{\partial X}\frac{\partial P}{\partial X}+C\frac{\partial^2 P}{\partial X^2}+\frac{\partial D}{\partial Y}\frac{\partial P}{\partial Y}+D\frac{\partial^2 P}{\partial Y^2} = U*\left(\phi_c \frac{\partial H}{\partial X}+\sigma*\frac{\partial \phi_s}{\partial X}\right)+\beta\,\phi_c \frac{\partial H}{\partial T} \tag{3.15}$$

is obtained. Naming derivatives of C and D as:

$$DC = \frac{\partial C}{\partial X} \tag{3.16}$$

$$DD = \frac{\partial D}{\partial Y} \tag{3.17}$$

and writing the derivatives explicitly gives the following:

$$DC = H^3 \frac{\partial \phi_x}{\partial X} + 3 H^2 \phi_x \frac{\partial H}{\partial X} \tag{3.18}$$

$$DD = H^3 \frac{\partial \phi_y}{\partial Y} + 3 H^2 \phi_y \frac{\partial H}{\partial Y} \tag{3.19}$$

Therefore non-dimensional modified Reynolds equation can be expressed in the most explicit form as:

$$DC\frac{\partial P}{\partial X} + C\frac{\partial^2 P}{\partial X^2} + DD\frac{\partial P}{\partial Y} + D\frac{\partial^2 P}{\partial Y^2} = U^*\phi_c\frac{\partial H}{\partial X} + U^*\sigma^*\frac{\partial \phi_s}{\partial X} + \beta\phi_c\frac{\partial H}{\partial T} \tag{3.20}$$

At this stage, finite differencing substitutions are introduced to Eq. (3.20). For any given property, Ψ, first and second derivatives in X and Y-directions can be written as given in Eq.s (3.21-24), using the notations shown in Figure 3.1 where *W*, *E*, *S* and N stand for, respectively, west, east, south and north neighboring nodes of node *P*.

$$\frac{\partial \Psi}{\partial X} = \frac{\Psi_{i+1,j} - \Psi_{i-1,j}}{2\,\Delta X} \tag{3.21}$$

$$\frac{\partial \Psi}{\partial Y} = \frac{\Psi_{i,j+1} - \Psi_{i,j-1}}{2\,\Delta Y} \tag{3.22}$$

$$\frac{\partial^2 \Psi}{\partial X^2} = \frac{\Psi_{i+1,j} - 2\,\Psi_{i,j} + \Psi_{i-1,j}}{(\Delta X)^2} \tag{3.23}$$

$$\frac{\partial^2 \Psi}{\partial Y^2} = \frac{\Psi_{i,j+1} - 2\,\Psi_{i,j} + \Psi_{i,j-1}}{(\Delta Y)^2} \tag{3.24}$$

Applying the differencing scheme to the derivatives in Eq.s (3.18-20),

$$DC\frac{P_{i+1,j}-P_{i-1,j}}{2\varDelta X}+C\frac{P_{i+1,j}-2P_{i,j}+P_{i-1,j}}{\left(\varDelta X\right)^{2}}+DD\frac{P_{i,j+1}-P_{i,j-1}}{2\varDelta Y}+D\frac{P_{i,j+1}-2P_{i,j}+P_{i,j-1}}{\left(\varDelta Y\right)^{2}}$$

$$=U^{*}\phi_{c}\frac{H_{i+1,j}-H_{i-1,j}}{2\varDelta X}+U^{*}\sigma^{*}\frac{\phi_{s_{i+1,j}}-\phi_{s_{i-1,j}}}{2\varDelta X}+\beta\phi_{c}\frac{\partial H}{\partial T} \tag{3.25}$$

is obtained where

$$DC = H_{i,j}^{3}\frac{\phi_{x_{i+1,j}}-\phi_{x_{i-1,j}}}{2\,\varDelta X}+3\,H_{i,j}^{2}\,\phi_{x}\,\frac{H_{i+1,j}-H_{i-1,j}}{2\,\varDelta X} \tag{3.26}$$

$$DD = H_{i,j}^{3}\frac{\phi_{y_{i,j+1}}-\phi_{y_{i,j-1}}}{2\,\varDelta Y}+3\,H_{i,j}^{2}\,\phi_{y}\,\frac{H_{i,j+1}-H_{i,j-1}}{2\,\varDelta Y} \tag{3.27}$$

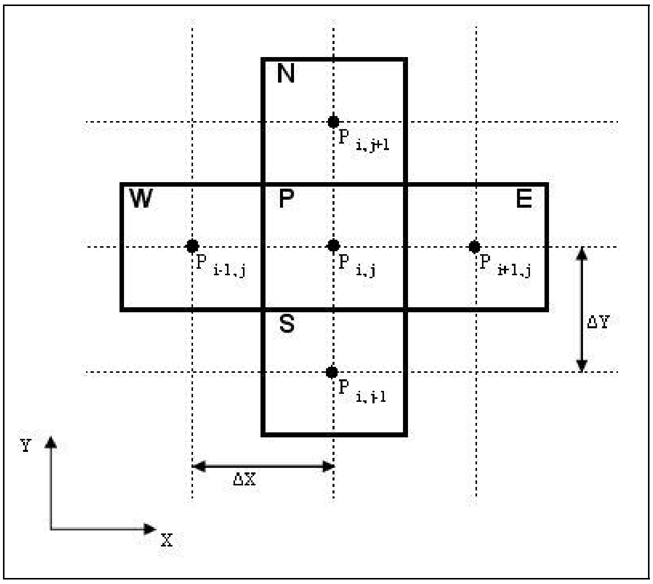

Figure 3.1 : Notation for the nodes

The last term in Eq. (3.25) is the non-dimensional squeeze film velocity. It can be discretized using the previous local thickness values and non-dimensional time increment to obtain:

$$\frac{\partial H^{(t)}}{\partial T} = \frac{H_{i,j}^{(t)}-H_{i,j}^{(t-\Delta t)}}{\varDelta T} \tag{3.28}$$

H, ϕ_c, squeeze film velocity and flow factors can all be calculated once the orientation of the piston is known or predicted. ΔX, ΔY, U^*, σ^* and β can already be found simply from inputs. Therefore, Eq. (3.25) can be solved for the pressure distribution employing an iterative technique. For the simplicity of the remaining calculations, Eq. (3.25) can be arranged to form the general equation:

$$AW_{i,j}\, P_{i-1,j} + AE_{i,j}\, P_{i+1,j} + AS_{i,j}\, P_{i,j-1} + AN_{i,j}\, P_{i,j+1} + AP_{i,j}\, P_{i,j} = S_{i,j} \tag{3.29}$$

where

$$AW_{i,j} = -\frac{H_{i,j}}{4\,(\Delta X)^2}\left[H_{i,j}^{\,2}\left(\phi_{x_{i+1,j}} - 4\,\phi_{x_{i,j}} - \phi_{x_{i-1,j}}\right) + 3\,\phi_{x_{i,j}}\left(H_{i+1,j} - H_{i-1,j}\right)\right] \tag{3.30}$$

$$AE_{i,j} = \frac{H_{i,j}}{4\,(\Delta X)^2}\left[H_{i,j}^{\,2}\left(\phi_{x_{i+1,j}} + 4\,\phi_{x_{i,j}} - \phi_{x_{i-1,j}}\right) + 3\,\phi_{x_{i,j}}\left(H_{i+1,j} - H_{i-1,j}\right)\right] \tag{3.31}$$

$$AS_{i,j} = -\frac{H_{i,j}}{4\,(\Delta Y)^2}\left[H_{i,j}^{\,2}\left(\phi_{y_{i,j+1}} - 4\,\phi_{y_{i,j}} - \phi_{y_{i,j-1}}\right) + 3\,\phi_{y_{i,j}}\left(H_{i,j+1} - H_{i,j-1}\right)\right] \tag{3.32}$$

$$AN_{i,j} = \frac{H_{i,j}}{4\,(\Delta Y)^2}\left[H_{i,j}^{\,2}\left(\phi_{y_{i,j+1}} + 4\,\phi_{y_{i,j}} - \phi_{y_{i,j-1}}\right) + 3\,\phi_{y_{i,j}}\left(H_{i,j+1} - H_{i,j-1}\right)\right] \tag{3.33}$$

$$AP_{i,j} = -2\,H_{i,j}^{\,3}\left(\frac{\phi_{x_{i,j}}}{(\Delta X)^2} + \frac{\phi_{y_{i,j}}}{(\Delta Y)^2}\right) \tag{3.34}$$

$$S_{i,j} = \frac{U^*}{\Delta X}\left[\phi_{c_{i,j}}\left(H_{i+1,j} - H_{i-1,j}\right) + \sigma^*\left(\phi_{c_{i+1,j}} - \phi_{c_{i-1,j}}\right)\right] + \beta\phi_{c_{i,j}}\,\frac{H_{i,j}^{\,(t)} - H_{i,j}^{\,(t-\Delta t)}}{\Delta T} \tag{3.35}$$

In order to solve the general equation, a (mxn) mesh is generated over the skirt surface. Assuming there is no motion of the piston along the pin axis, a symmetry plane for the lateral motion of the piston can be defined perpendicular to pin axis passing through the origin of the coordinate system which is moving with the piston as shown in Figure 3.2.

Lubricated surface of a conventional ICE piston skirt is not a full cylinder. A meshed skirt is shown in Figure 3.3, with angle of lubricated region being denoted by θ_{lub}. However, cylindrical ringless pistons are also used in small reciprocating compressors. In order to obtain a general model, the piston skirt is taken as a fully-lubricated perfect cylinder. Making use of the symmetry, half of the skirt surface is meshed to save computation time. The half-cylindrical surface is transformed to a plane surface with the following relation:

$$x = z \tag{3.36}$$

$$y = r\theta \tag{3.37}$$

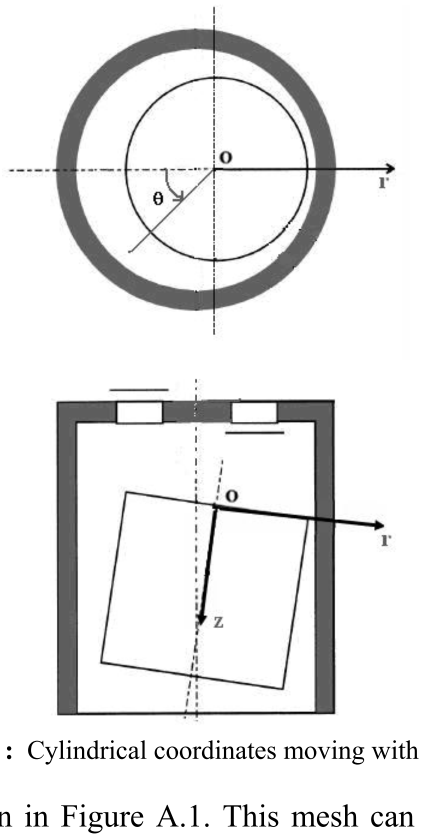

Figure 3.2 : Cylindrical coordinates moving with the piston

The general mesh is given in Figure A.1. This mesh can be adopted for use in an ICE piston solution by simply defining the nodes outside the lubricated region, setting the pressures at these nodes to crankcase pressure and carrying out the iterations only at the nodes within the lubricated region. A modified mesh example is shown in Figure A.2. Nodal coordinates for a (mxn) mesh will be denoted with i and j such that:

$$i = 1 , 2 , ... , m-1 , m \tag{3.38}$$

$$j = 1 , 2 , ... , n-1 , n \tag{3.39}$$

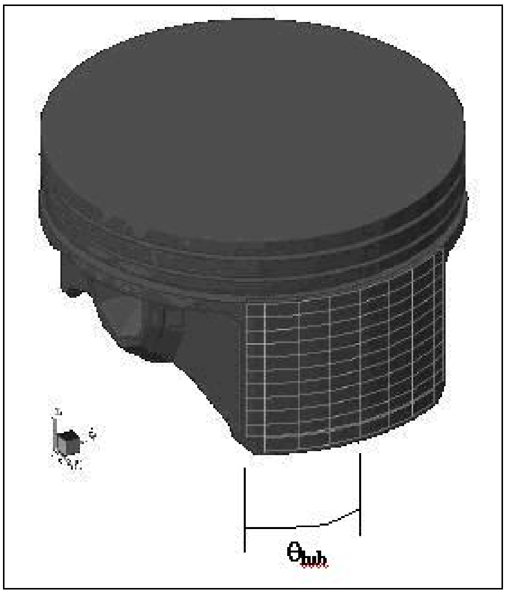

Figure 3.3 : Lubricated surface and mesh without the symmetry plane for a conventional ICE piston skirt (one side is shown)

Pressure values at $x = 0$ and $x = L$ are set to pressure values, respectively, p_1 and p_2, which will be switched to be used as leading and trailing edge pressures depending on the direction of instantaneous piston motion. At the nodes on the symmetry lines, there is no flow in y-direction, leading to zero pressure gradient. Thus, south and north neighboring nodes have equal pressure values. For the (mxn) domain in the solution of cylindrical piston, these conditions can be written in non-dimensional form as follows:

$$\text{at } X = 0, \quad P_{1,j} = P_1 \tag{3.40}$$

$$\text{at } X = 2, \quad P_{m,j} = P_2 \tag{3.41}$$

$$\text{for}\quad Y = 0,\qquad \frac{\partial P}{\partial Y} = 0\ \text{, thus}\quad P_{i\ ,\ 2n-2} = P_{i\ ,\ 2} \tag{3.42}$$

$$\text{for}\quad Y = 2\pi\frac{r}{L},\qquad \frac{\partial P}{\partial Y} = 0\ \text{, thus}\quad P_{i\ ,\ n+1} = P_{i\ ,\ n\text{-}1} \tag{3.43}$$

For the domain in the solution of ICE piston, in addition to these, the following conditions can be applied:

$$\text{for}\quad Y = 2\theta_{\text{lub}}\frac{r}{L},\qquad P_{i\ ,\ n_{\text{lub}}} = P_2 \tag{3.44}$$

$$\text{for}\quad Y = 2\left(\pi-\theta_{\text{lub}}\right)\frac{r}{L},\qquad P_{i\ ,\ (n\text{-}n_{\text{lub}}+1)} = P_2 \tag{3.45}$$

$$\text{for}\quad 2\theta_{\text{lub}}\frac{r}{L} < Y < 2\left(\pi-\theta_{\text{lub}}\right)\frac{r}{L},$$

$$P_{i\ ,\ n_{un\,\text{lub}}} = P_2 \qquad n_{un\,\text{lub}} = n_{\text{lub}}+1, n_{\text{lub}}+2, ..., n\text{ - }n_{\text{lub}}\text{ - }1, n\text{ - }n_{\text{lub}} \tag{3.46}$$

where n_{lub} is the node corresponding to θ_{lub} that defines the boundary of the lubricated skirt area. n_{lub} can be found in MATLAB language by:

$$n_{\text{lub}} = floor\left(\theta_{\text{lub}}\frac{n\text{ - }1}{\pi}\right)+1 \tag{3.47}$$

Pressure distribution is calculated using Gauss-Seidel iteration. Initial condition is defined as a linear distribution along X-direction, between $P_{1,j}$ and $P_{m,j}$ which are P_1 and P_2 respectively. After the calculation of a new value at each node, it is checked for the error. Overall convergence is achieved only if local convergence at each node is satisfied. A pseudo-code is given in Figure 3.4.

```
sor = 1;              % can be changed for over or under-relaxation, sor = 1 means no relaxation
dummy = 1;
while dummy>0
  dummy = 0;
    for j = 1:n
      for i = 2:nodalcavboun(j)-1
        pnew(i,n) = (S(i,n)-AW(i,n)*pold(i-1,n)-AE(i,n)*pold(i+1,n)-AS(i,n)*pold(i,n-1))/AP(i,n);
        pnew(i,j) = sor*pnew(i,j)+(1-sor)*pold(i,j);              % relaxation step
        if abs((pnew(i,j)-pold(i,j))/pnew(i,j)) > err              % error check
          dummy = 1;
        end
      pold(i,j) = pnew(i,j);
    end
  end
end
```

Figure 3.4 : Pseudo-code for pressure iteration

3.3 Determination of Cavitation Boundary

Film rupture is assumed to occur satisfying the modified Reynolds film separation condition. Details were given in Section 2.2.2.2 for a one-dimensional flow. Reynolds cavitation proposes no-flow across the cavitation boundary. In a two-dimensional solution, Reynolds (Swift-Steiber) boundary conditions are:

$$\text{at node } \left(i_c, j_c\right), \qquad P = P_2 \ , \ \frac{\partial P}{\partial X} = 0 \ , \ \frac{\partial P}{\partial Y} = 0 \tag{3.48}$$

Integrating Reynolds equation and applying the BCs to find the integration constants would complicate the solution in a two-dimensional domain. Instead, in this study, it was preferred to find the cavitation boundary through iteration. The iteration was based on detecting the nodes with pressures below trailing edge pressure and shifting the outlet node against flow direction until pressures lower than P_T are eliminated. No-flow boundary condition was satisfied when the west (or south) node pressure was found to be equal or higher than the outlet node pressure, P_T, while piston was moving towards TDC (or BDC). A sketch showing the iteration for cavitation boundary is given in Figure 3.5.

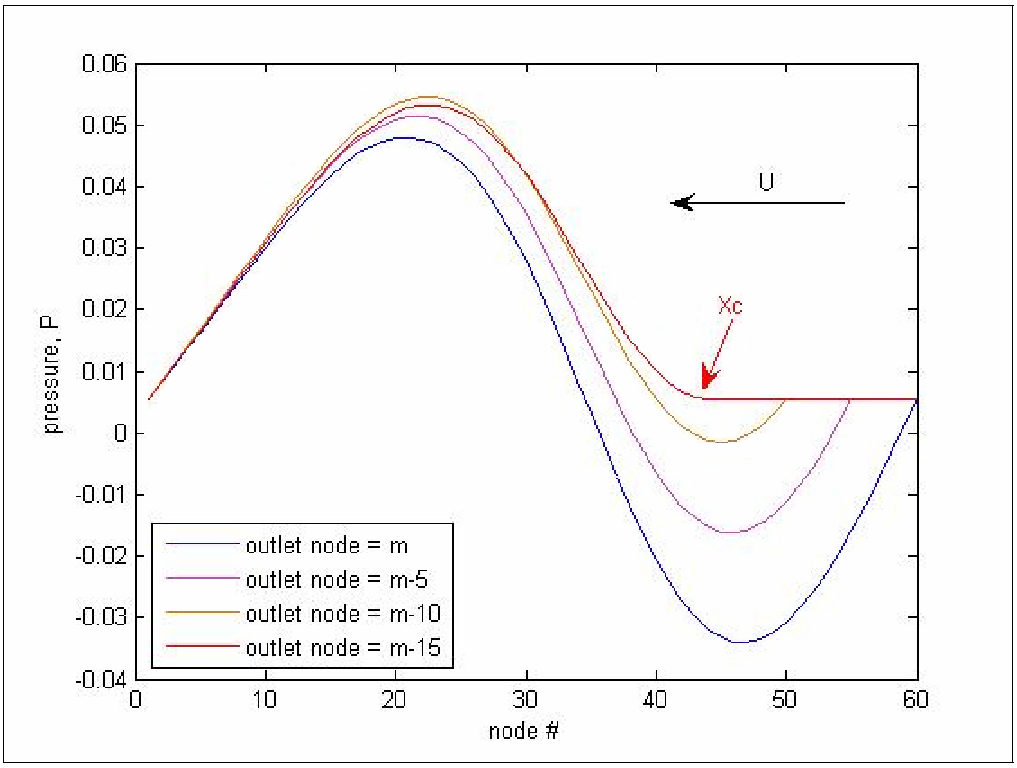

Figure 3.5 : Change in pressure distribution with marching outlet location

As a result of flow separation, the strip-like patterns of lubricant left beyond the cavitation boundary were neglected since in those areas, lubricant pressure was constant and equal to trailing edge outlet value as it was also the case inside cavitated zones. This way, mass conservation across the cavitation boundary was also satisfied.

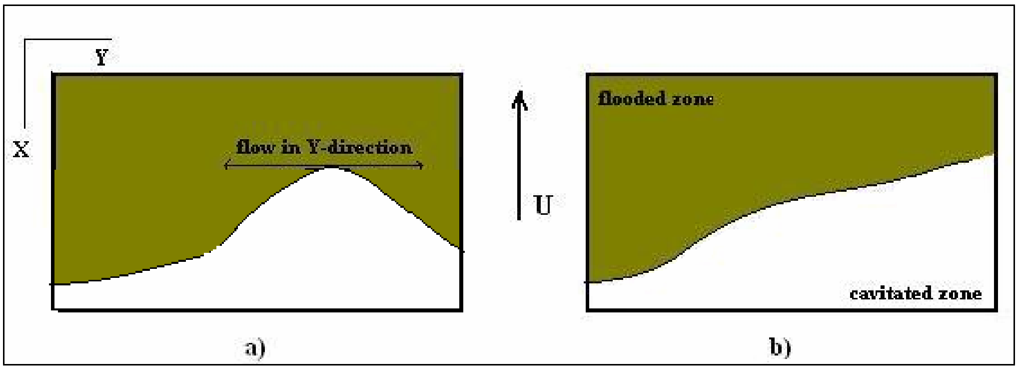

Figure 3.6 : Cavitation boundary characteristic a) violating the assumption of no-flow in Y-direction and b) expected

Once the no-flow condition is satisfied in X-direction, it will be satisfied in Y-direction, too. This can only be violated at a point shown in Figure 3.6a. However, the expected cavitation boundary behavior is approximately similar to that shown in Figure 3.6b, due to squeeze film effect which encourages additional pressure development at one side of the piston whilst causing a starvation effect at the other side.

3.4 Calculation of Local Film Thicknesses

Assumption of rigid bodies made the direct calculation of local film thickness possible, using the predicted eccentricities and skirt profile which was introduced to the model as a function of piston length as shown in Figure 4.6. Thickness at each node was calculated by:

$$h_{i,j} = c + \left(e_t - \left(e_t - e_b \right) \frac{z_{i,j}}{L} \right) \cos(\theta_{i,j}) + \Delta h_{i,j} \tag{3.49}$$

where $\Delta h_{i,j}$ is the deviation from nominal radius due to the profile.

3.5 Calculation of Forces and Moments

3.5.1 Lateral Pin Force

From kinematic analysis of piston and connecting rod assembly, piston axial velocity and acceleration, connecting rod axial and lateral accelerations and connecting rod tilt angle were written as functions of crank angle:

$$U = r_c \, \omega \left(\sin(\tau) + \frac{1}{2} \frac{r_c}{C_{MP}} \sin(2\tau) \right) \tag{3.50}$$

$$a_{pX} = r_c \, \omega^2 \left(\cos(\tau) - \frac{r_c}{C_{MP}} \cos(2\tau) \right) \tag{3.51}$$

$$A_{bZ} = r_c \, \omega \left(\cos(\tau) - \frac{1}{2} \frac{r_c}{C_{BM}} \cos(2\tau) \right) \tag{3.52}$$

$$A_{bX} = r_c\ \omega^2 \left(\frac{C_{BM}}{C_{MP}} - 1 \right) \sin(\tau) \tag{3.53}$$

$$\phi = \sin^{-1}\left(\frac{r_c}{C_{MP}} \sin(\tau) \right) \tag{3.54}$$

Gas force was calculated from combustion chamber pressure at each crank angle.

$$F_g = \pi\ r^2\ p_g \tag{3.55}$$

Discretized form of Eq. (2.34) was used to calculate friction force on piston skirt as:

$$F_f = -sign(U)\ 2 \sum f_{f_{i,j}} \tag{3.56}$$

where

$$f_{f_{i,j}} = \left[\frac{\mu |U|}{h_{i,j}} \left(\phi_{f_{i,j}} + (2\ V_{r1} - 1) \phi_{fs_{i,j}} \right) + \mu_f\, p_c \right] \Delta A \tag{3.57}$$

is nodal friction force and 2 is a multiplier due to the symmetric solution for half of skirt surface.

Pin lateral force was found by substituting the values from Eq. (3.49) and Eq. (2.25).

3.5.2 Normal Force

Normal force composed of hydrodynamic and asperity contact pressures were calculated as:

$$F_h = 2 \sum \left[f_{h_{i,j}}\ c\text{os}\left(\theta_{i,j}\right) \right] \tag{3.58}$$

where

$$f_{h_{i,j}} = \left(P_{i,j} + p_{c_{i,j}}\right) \Delta A \qquad (3.59)$$

is normal load on each node.

3.5.3 Moment due to Normal Force

M_h was calculated as:

$$M_h = 2 \sum\left[f_{h_{i,j}} \; c\,\mathrm{os}\left(\theta_{i,j}\right) \left(z_P - z_{i,j}\right)\right] \qquad (3.60)$$

3.5.4 Moment due to Friction Force

Finally, M_h was calculated as:

$$M_f = 2 \sum\left[f_{h_{i,j}} \; r \; \cos\left(\theta_{i,j}\right) \right] \qquad (3.61)$$

3.6 Solution for Piston Secondary Motion

At this stage, Eq.s (2.16) were used to find piston position, velocity and acceleration in lateral direction. The coefficients on the right hand side were known from inputs. Force and moment terms on the left hand side are functions of piston position and velocity, but the functional dependence was not known explicitly. Therefore, equations were solved through an iterative procedure.

Due to domination of squeeze film velocity in Reynolds equation, top and bottom velocities were marched. For a predicted piston lateral velocity at a time step, top and bottom eccentricities and accelerations were found using the known values from the previous time step:

$$e_t^{(t)} = e_t^{(t-\Delta t)} - \dot{e}_t^{(t)} \; \Delta t \qquad (3.62a)$$

$$e_b^{(t)} = e_b^{(t-\Delta t)} - \dot{e}_b^{(t)} \; \Delta t \qquad (3.62b)$$

$$\ddot{e}_t^{(t)} = \frac{\dot{e}_t^{(t)} - \dot{e}_t^{(t-\Delta t)}}{\Delta t} \quad (3.63a)$$

$$\ddot{e}_b^{(t)} = \frac{\dot{e}_b^{(t)} - \dot{e}_b^{(t-\Delta t)}}{\Delta t} \quad (3.63b)$$

For simplicity, iteration was run in crankangle domain, using the following relation:

$$\tau = \omega t \quad (3.64)$$

Form Eq. (3.49), time step was found as:

$$\Delta t = \frac{\Delta \tau}{\omega} \quad (3.65)$$

To start the iteration, two sets of initial conditions were introduced. First set included the positions and velocities for the initial previous time step which would be used to calculate the positions and accelerations for the initial current time step. This set can be represented as:

$$at \;\; t = 0, \quad e_t^{(t-\Delta t)} = 0, \quad e_b^{(t-\Delta t)} = 0, \quad \dot{e}_t^{(t-\Delta t)} = 0, \quad \dot{e}_b^{(t-\Delta t)} = 0 \quad (3.66)$$

The second set was the initial guess of velocities for the current time step:

$$at \;\; t = 0, \quad \dot{e}_t^{(t)} = 0, \quad \dot{e}_b^{(t)} = 0 \quad (3.67)$$

The code for the PSM iteration calculates lateral pin force, lateral skirt force and moments due to lateral and friction forces, F_{rX}, F_h, M_h and M_f, respectively, using the equations given in Section 3.5 for the guessed value of current position and checks Eq.s (2.16). Velocities for the current step are marched independently until both force and moment balance is reached. Once the velocities are found, together with the positions, they are set to be the previous values for the next step. When moved on to the next time step, the code uses the previous velocity values also as the current initial values to start the iteration. A pseudo-code for the iteration is given in Appendix B and the flow chart for the code is given in Appendix C.

4 RESULTS AND DISCUSSION

4.1 General Input Data

The model was run for a 9 lt., 6-cylinder diesel engine piston. General input data are given in Table 4.1

Table 4.1 : General input data

Input	Nomenclature	Value	Unit
r	piston radius	675	mm.
L	piston skirt length	828	mm.
Rc	crank radius	72	mm.
C	nominal clearance	20	μm.
C_{MP}	connecting rod length	221.5	mm.
C_{BM}	connecting rod mass center location	71.66	mm.
z_{CM}	piston mass center location	10.8	mm.
z_P	piston pin axis location	37.3	mm.
m_p	piston mass	1.55	kg.
I_p	piston moment of inertia	0.00307	kg.m^2
m_b	connecting rod mass	2.89	kg.
I_b	connecting rod moment of inertia	0.02815	kg.m^2
ω	crank speed	157.08	rad/sec
σ_1	piston surface roughness	0.80	μm.
σ_2	bore surface roughness	0.47	μm.
γ_1	piston surface roughness orientation factor	1	-
γ_2	bore surface roughness orientation factor	1	-
h_{max}	supply oil film thickness	10	μm.
-	oil type	SAE 5W/30	-
μ	viscosity (at 70ºC)	0.023	Pa.s
μ_f	dry friction coefficient	0.3	-

4.2 Pressure Distribution

Pressure distributions over the skirt surface for two crank positions are given in Figure 4.2 and Figure 4.4.

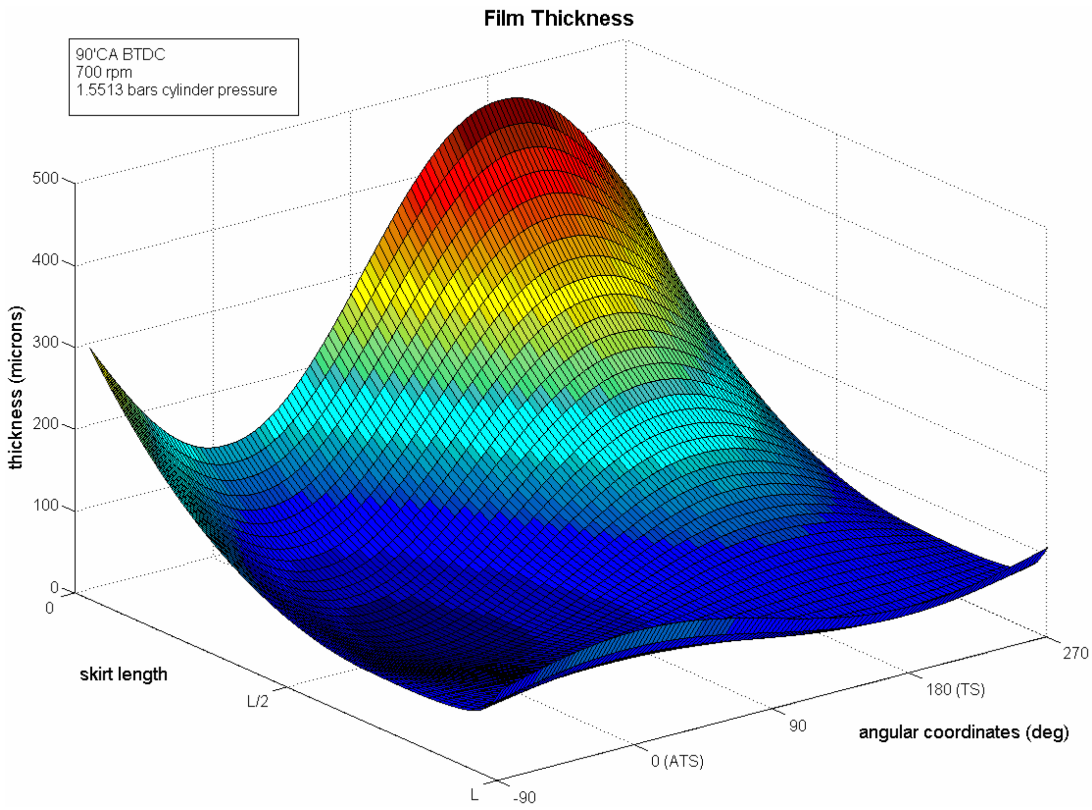

Figure 4.1 : Film thickness at 90ºCA BTDC

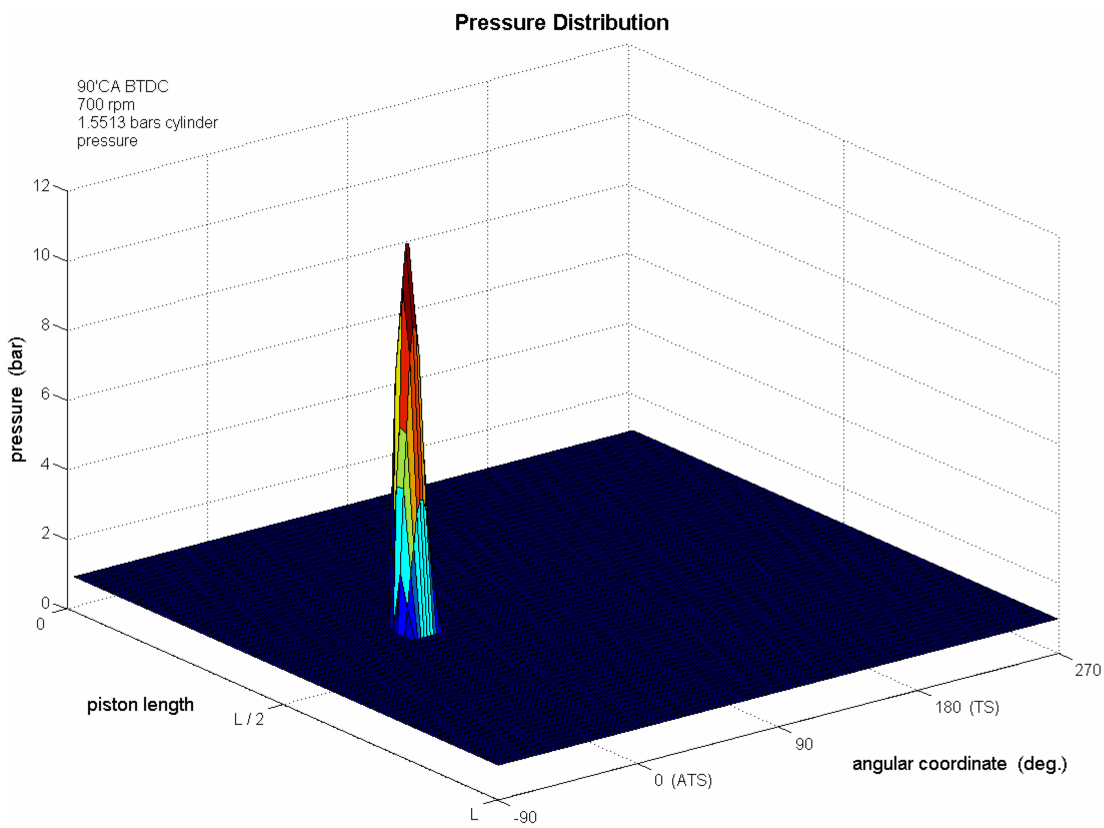

Figure 4.2 : Pressure distribution at 90ºCA BTDC

Pressure distributions over the skirt surface for two crank positions are presented in Figure 4.2 and Figure 4.4 to give an idea of the solutions.

Figure 4.2 is for pressure at 90ºCA before firing TDC. In Figure 4.1, instantaneous gap between the skirt and cylinder wall is given. At this crankangle position, the minimum thickness region can be seen on ATS. Therefore ATS was lubricated and pressure development was on this side (Figure 4.2).

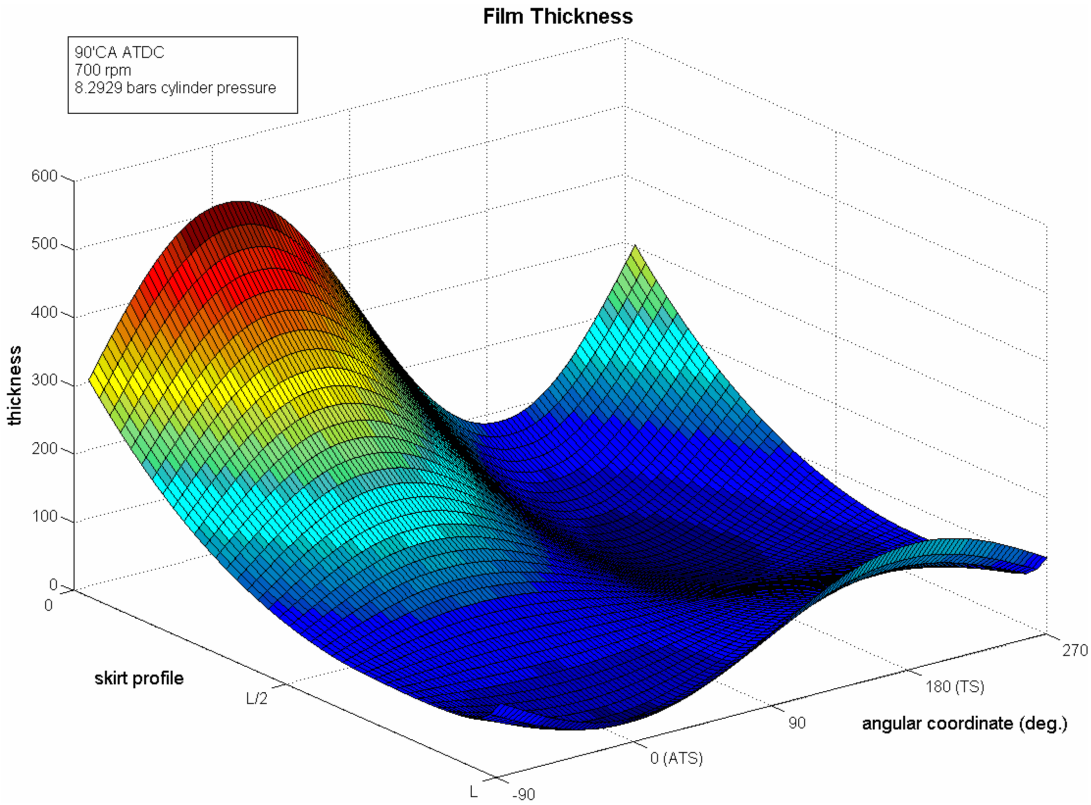

Figure 4.3 : Film thickness at 90ºCA ATDC

Figure 4.3 shows the gap and Figure 4.4 shows the pressure distribution at 90ºCA after firing TDC. At this crankangle, piston was forced towards the TS, where minimum thickness region and fluid film development can be seen on this side.

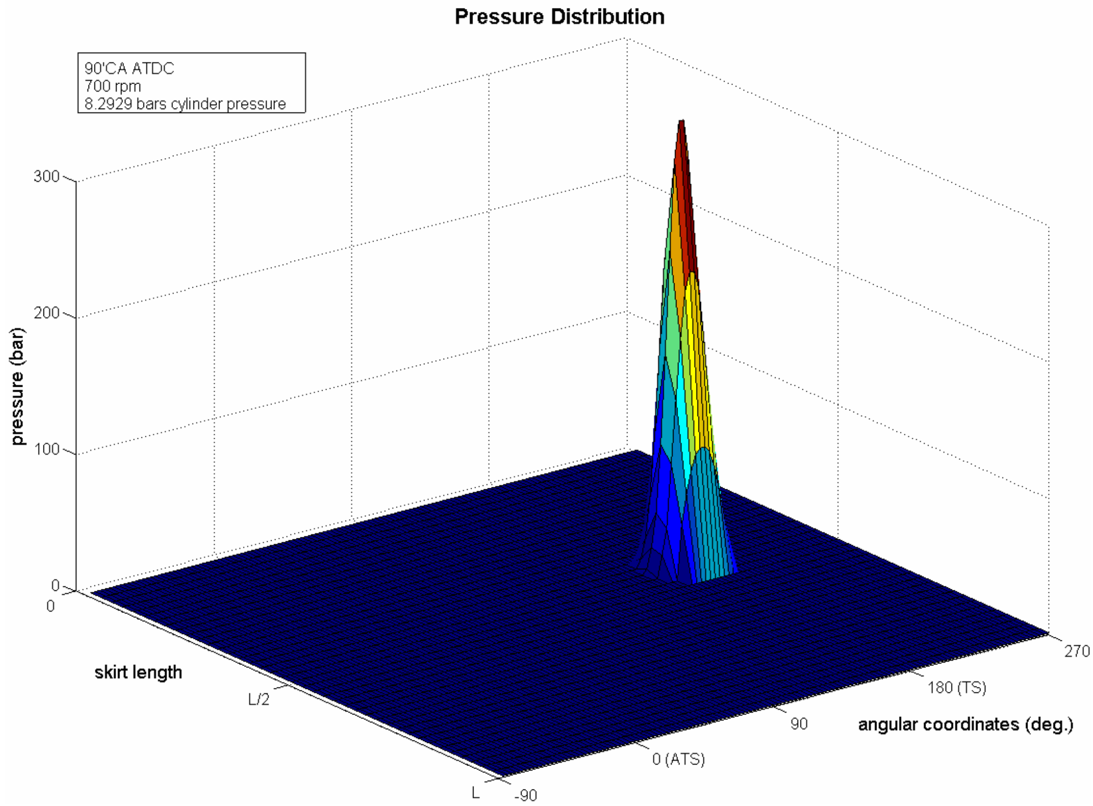

Figure 4.4 : Pressure distribution at 90ºCA ATDC

4.3 Secondary Motion of the Piston

Major result of the PSD code was piston lateral position inside the cylinder. In Figure 4.5, lateral displacement of piston top and bottom from the cylinder axis when the piston is around the firing TDC are shown.

Piston top moves from thrust side to anti-thrust side at the beginning of the compression stroke and back to thrust side after the piston passes from the firing TDC. On the other hand, piston bottom moves from ATS to TS at the beginning of the compression stroke and back to ATS after the firing TDC. These trends for the lateral displacement were expected. However, the displacements of top and bottom towards opposite sides were not expected. This indicates a high tilting of the piston which is not a desired condition.

The reason that the tilt of piston resulted in high values is the barrel profile. As seen in Figure 4.6, pin, which is the rotation axis, is located over the plain section of the skirt profile. Hydrodynamic force first develops at this plain section as the piston approaches to cylinder wall causing the piston to tilt. It increases until the hydrodynamic force moves towards pin axis until the moment balance is reached.

This behavior got more important in this study since piston and cylinder were taken as rigid, letting no deformation which could actually help the piston to improve its smooth operation by decreasing its need to tilt.

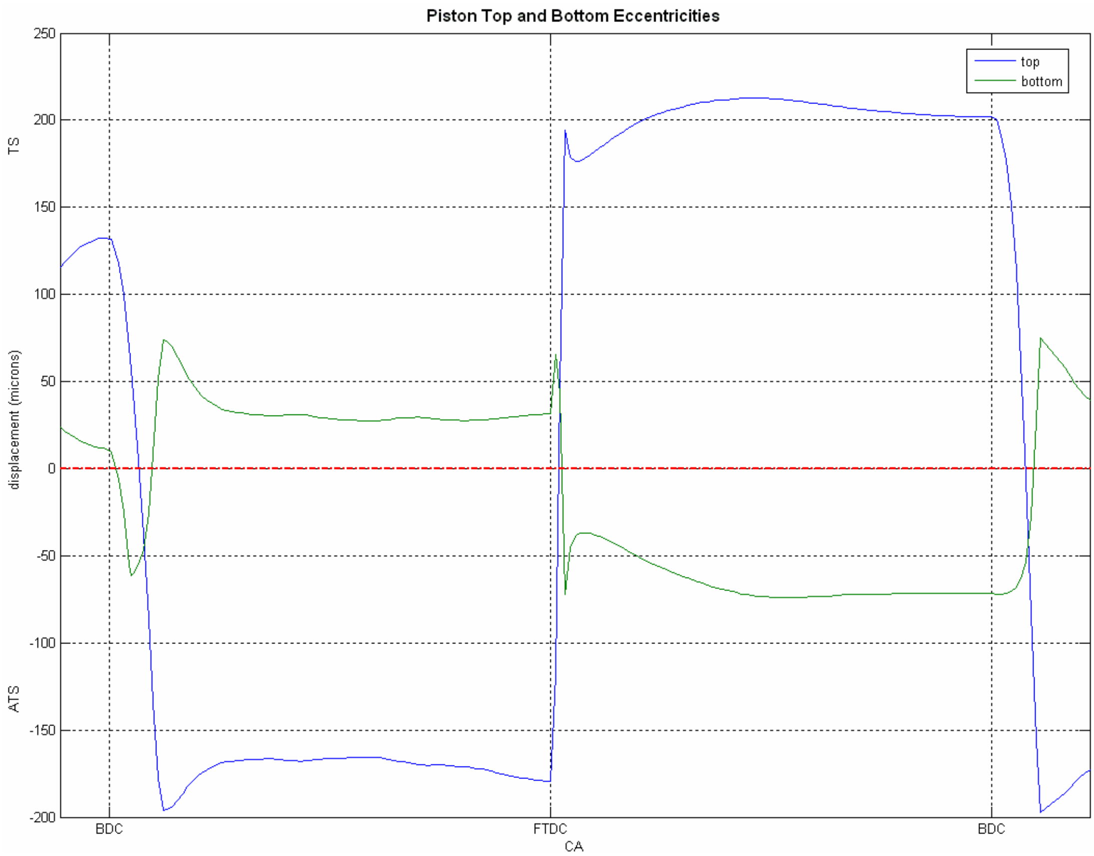

Figure 4.5 : Lateral displacement of piston top and bottom from cylinder axis

To decrease the tilt under these conditions, the plain section and pin location should be designed to coincide. Moving pin axis away from the mass center will effect in a negative manner since the inertia force develops at piston center of mass. Therefore skirt barrel profile should be modified moving the plain section towards the pin axis.

Lubricated side of the piston at each crankangle can be better seen in Figure 4.7. Piston slides on its ATS during compression stroke and on its TS during expansion stroke, as expected. In Figure 4.8, piston tilt is given.

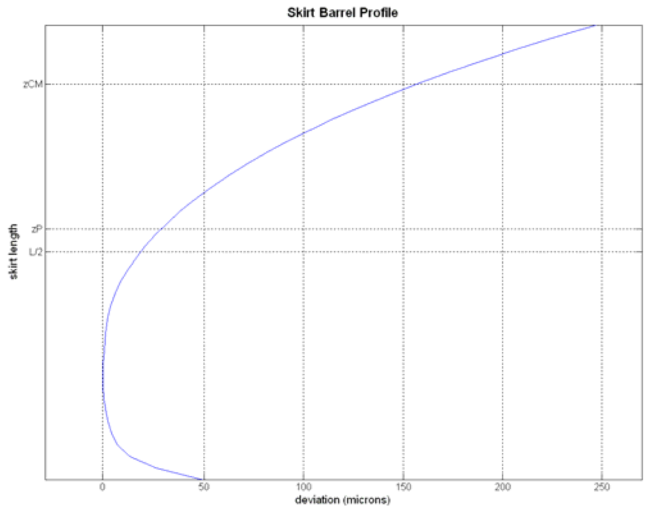

Figure 4.6 : Skirt barrel profile

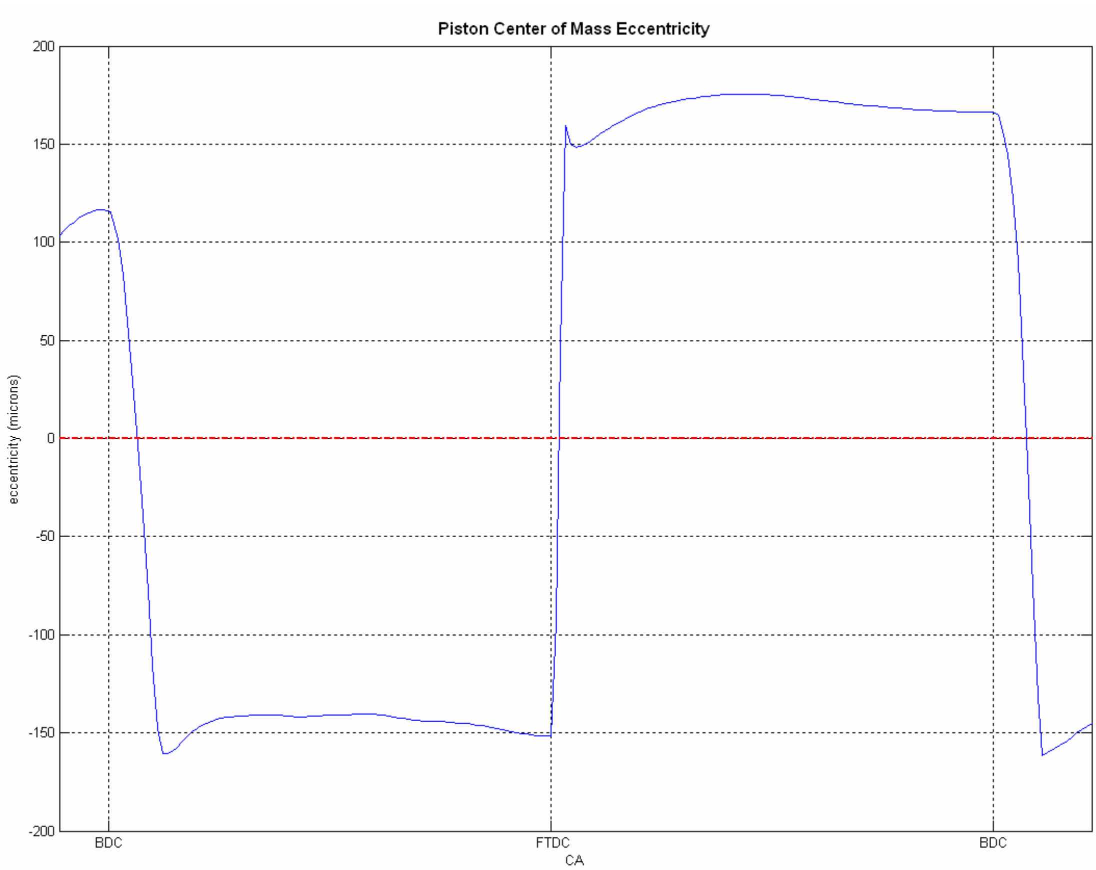

Figure 4.7 : Lateral displacement of piston mass center from cylinder axis

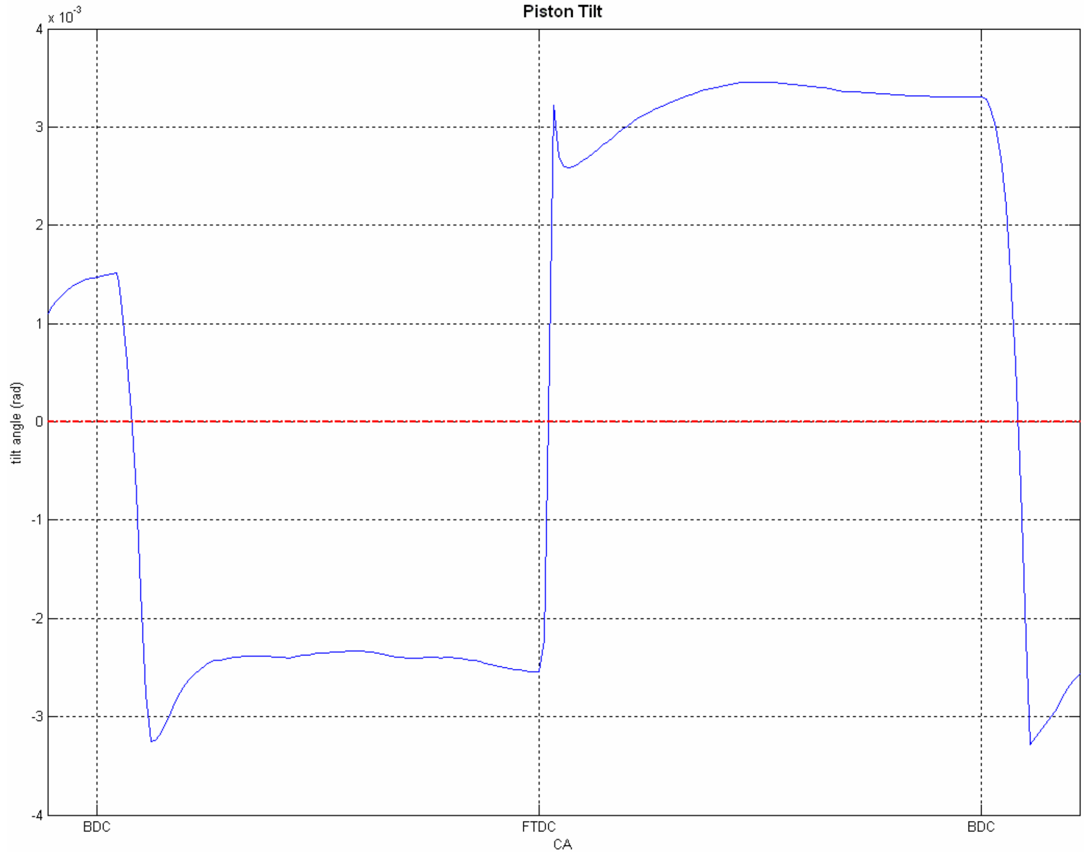

Figure 4.8 : Piston tilt

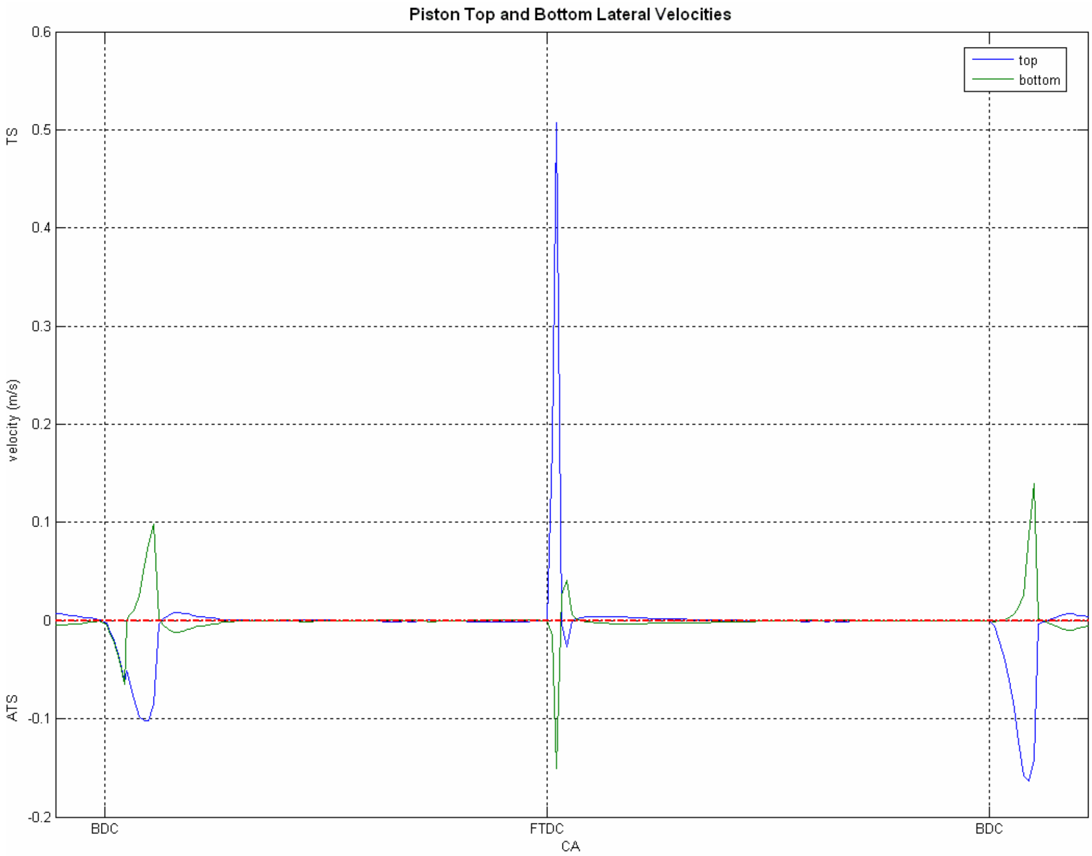

Figure 4.9 : Lateral velocities of piston top and bottom

Lateral velocities of top and bottom (Figure 4.9) were close to zero except the disturbances just after the piston passed TDCs.

Normal and friction forces acting on the piston skirt and friction power loss are given in Figure 4.10, Figure 4.11 and Figure 4.12. Lateral force was calculated to be higher after firing TDC due to the increase in combustion chamber pressure. Friction also increases with increasing gas pressure. In the there figures, hydrodynamic forces and power loss were plotted with dashed lines. For both lateral and friction forces, total forces were found to be greater than the forces caused by hydrodynamic effects, not during the entire cycle but only at some crankangle degrees. The reason for this difference is the asperity contact occurring only around firing TDC when the combustion chamber pressure was very high. Asperity contact resulted in an increase in both lateral and friction forces applied on the piston skirt.

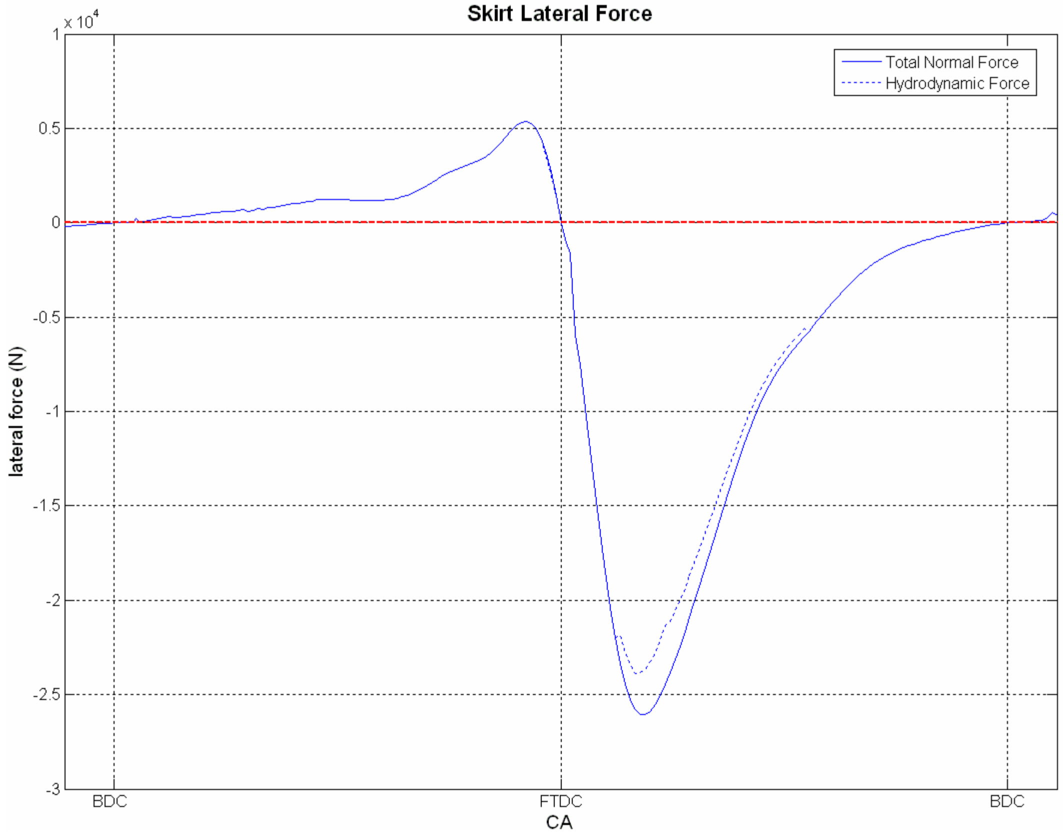

Figure 4.10 : Lateral force carried by piston skirt

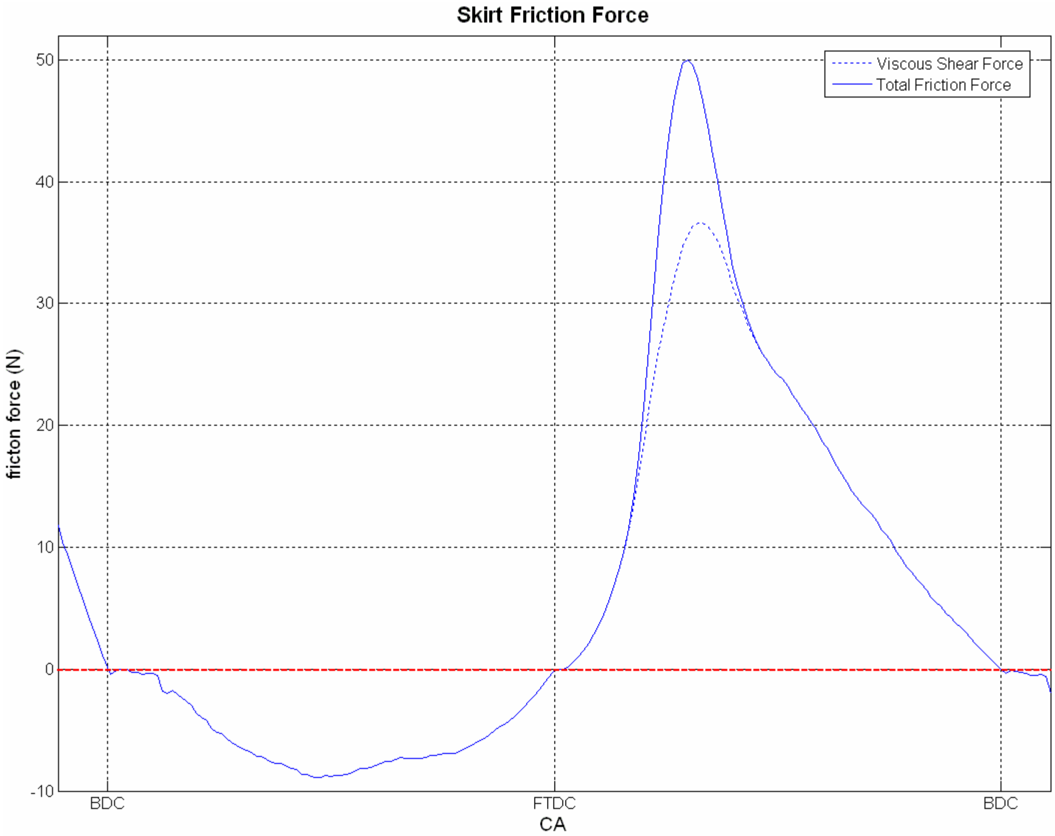

Figure 4.11 : Friction force acting on the piston skirt

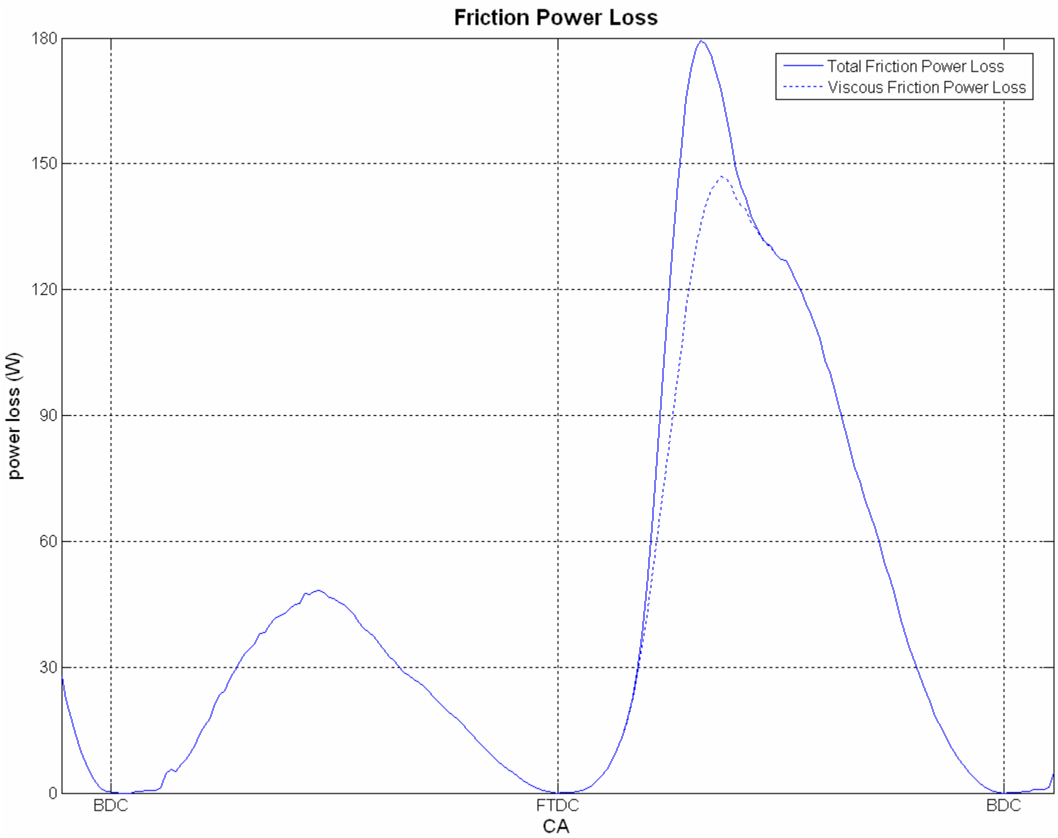

Figure 4.12 : Power loss due to skirt friction

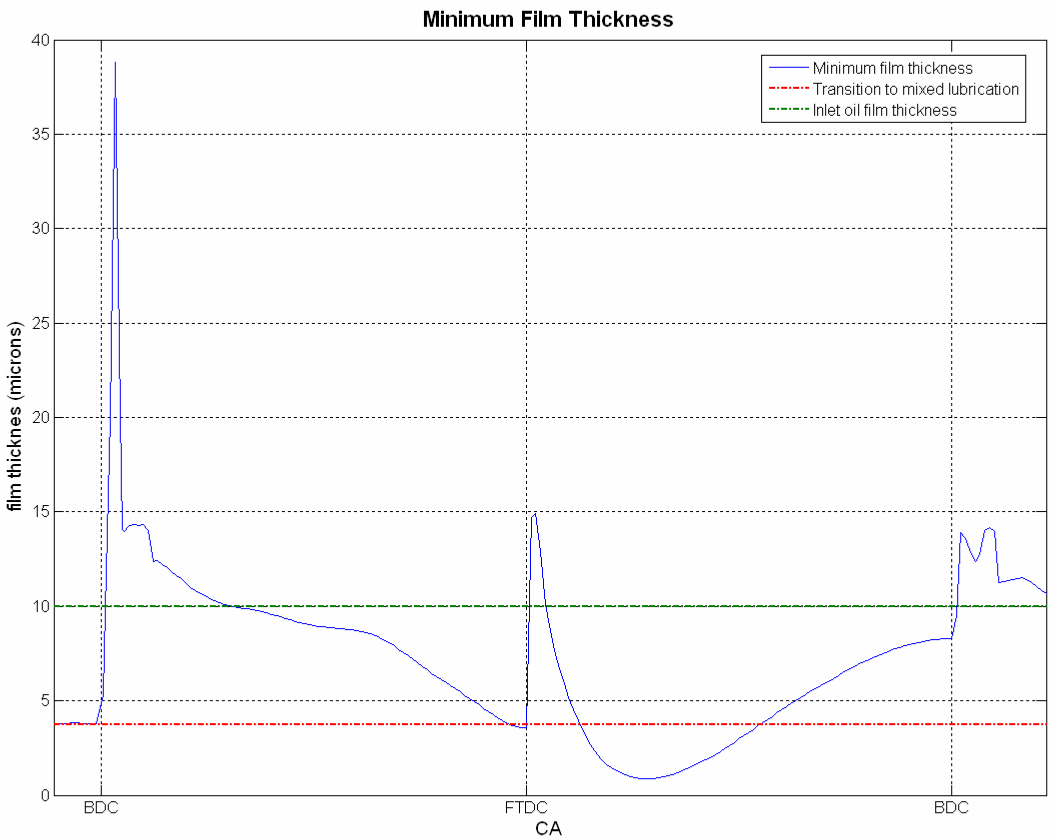

Figure 4.13 : Minimum film thickness

Asperity contact regions can be seen more clearly in Figure 4.13 where minimum film thickness is plotted against crankangle. In the figure, red dashed line indicates the transition limit from hydrodynamic to mixed lubrication. This limit is defined as $H_\sigma = 4$, corresponding to a film thickness of $h = 3.71\ \mu m$. In the model, asperity contact calculations were added to the solution only at locations where film thickness dropped under this limiting value. After the firing TDC, asperity contact affects significantly for a crankangle range of 80º between approximately 200 and 280 ºCA. In addition to this, for about 10ºCA before TDC, a slight asperity contact was calculated. However, this contact was so weak that it caused very small increase in lateral and friction force, which could not be noticed in Figure 4.10 and Figure 4.11.

The green line in Figure 4.13 is supply inlet thickness, $h_{max} = 10\ \mu m$. It is seen that after DCs, minimum film thickness values stayed over the green line for a certain crankangles meaning that no fluid film was generated on skirt surface while the piston is moving from one side of the cylinder to the other.

5 CONCLUSION

In this study, a mathematical model was constructed to investigate secondary motion of a reciprocating piston of an internal combustion engine. The model focused on the piston skirt in mixed lubrication. For hydrodynamic fluid pressure, Reynolds equation modified with flow factors was solved by finite differencing in order to take into account the effects of surface roughness on the two-dimensional flow of the lubricant between the skirt and liner surfaces. An asperity contact approach for the interaction of two rough surfaces was incorporated into the model to add the contribution of solid contact to hydrodynamic load on piston skirt and to viscous friction. Fluid film rupture locations were also found through iteration assuming flow separation at the outlet.

Following the skirt lubrication solution, forces acting on the piston were determined and orientation of the piston with respect to the cylinder axis was calculated for each crankangle within the range of interest.

Beside the characteristics of lubrication and PSD analysis, friction force, power loss due to friction, critical crank positions where asperity contact occurs were also investigated.

To conclude, it was proved that the model could give reasonable results for the secondary motion of a piston with its skirt being in mixed lubrication. By the help of such a model, piston skirt lubrication characteristics including cavitation, surface texture, skirt profile and material properties, and frictional behavior of a piston skirt can be analyzed. This brings the opportunity to use the model, with further improvements and optimization, as a tool to assist in piston and liner design.

6 FURTHER STUDY

As the forthcoming studies on the subject, first of all, the code will be optimized for better computational efficiency.

The model will be improved such that it will be able to account for elastic and thermal deformations and to respond thermal variations throughout the engine cycle. It will also be integrated to a piston ring dynamics model.

The model will also be used in the research for the effects of macroscale surface finish and nanoparticle additives in oil on lubrication characteristics.

REFERENCES

[1] **Priest, M. And Taylor, C. M.**, 2000. Automobile engine tribology, Wear, **241**, 193-203.

[2] **Greenwood, I. A. and Tripp, J. H.**, 1971. The contact of two nominally flat surfaces, Proc. IMechE., **185**, 625-633.

[3] **Patir, N. and Cheng, H. S.**, 1978. An average flow model for determining effects of three-dimensional roughness on partial hydrodynamic lubrication, ASME Journal of Lubrication Technology, **100**, 12-17.

[4] **Patir, N. and Cheng, H. S.**, 1979. Application of average flow model to lubrication between rough sliding surfaces, Transactions of ASME, **101**, 220-230.

[5] **Zhu, D., Cheng, H.S., Arai, T. and Hamai, K.**, 1991. A numerical analysis for piston skirts in mixed lubrication - part I: Basic modeling, ASME Paper 91-Trib-66, STLE/ASME Tribology Conference, St. Louis.

[6] **Keribar, R. and Dursunkaya, Z**., 1992. A comprehensive model of piston skirt lubrication, SAE 920483.

[7] **Dursunkaya, Z. and Keribar, R.**, 1992. Simulation of secondary dynamics of articulated and conventional piston assemblies, SAE 920484.

[8] **Dursunkaya, Z., Keribar, R. and Ganapathy, V.**, 1994. A model of piston secondary motion and elastohydrodynamic skirt lubrication, ASME Journal of Tribology, **116**, 777-785.

[9] **Wong, V. W., Tian, T., Lang, H., Ryan, J. P., Sekiya, Y., Kobayashi, Y. and Aoyama, S.**, 1994. A numerical model of piston secondary motion and piston slap in partially flooded elastohydrodynamic skirt lubrication, SAE 940696.

[10] **Mansouri, S. H. and Wong, V. W.**, 2004. Effects of piston design parameters on piston secondary motion and skirt-liner friction, SAE 2004-01-2911.

[11] **Kimura, T., Takahashi, K. and Sugiyama S.**, 1994. Development of a piston secondary motion analysis program with elastically deformable piston skirt, SAE 1999-01-3303.

[12] **Etsion, I. and Gommed, K.**, 1995. Improved design with non-cylindrical profiles of gas-lubricated ringless piston, ASME Journal of Tribology, **117**, 143–147.

[13] **Prata, A. T., Fernandes, J. R. S. and Fagotti, F.**, 2000. Dynamic analysis of piston secondary motion for small reciprocating compressors, Transactions of ASME, **122**, 752-760.

[14] **Yang, J., Yang, W., Yu, X. and Wang, C.**, 2001. Design of internal combustion engine piston based on skirt lubrication analysis, SAE 2001-01-2486

[15] **Scholz, B. and Bargende, M.**, 2001. A hydrodynamic contact algorithm, SAE 2001-01-3596.

[16] **Duyar, M., Bell. D. and Perchanok, M.**, 2005. A comprehensive piston skirt lubrication model using a mass conserving EHL algorithm, SAE 2005-01-1640.

[17] **Chung, Y., Schock, H. J. and Brombolich, L. J.**, 1993. Fire ring wear analysis for a piston engine, SAE 930797.

[18] **Yun, J. E., Chung, Y., Chun, S. M. and Lee, K. Y.**, 1995. An application of simplified average Reynolds equation for mixed lubrication analysis of piston ring assembly in an internal combustion engine, SAE 952562.

[19] **Yu, B., Sawicki, J. T. and Dunaevsky, V.**, 1999. Analytical solution of piston ring pack lubrication for truck air brake compressor, SAE 1999-01-3769.

[20] **Stanley, R., Taraza, D., Henein, N. and Bryzik, W.**, 1999. A simplified friction model of the piston ring assembly, SAE 1999-01-0974.

[21] **Zhang, Y., Chen, G. and Li, B.**, 1999. Two-dimensional numerical analysis of piston ring lubrication of an internal combustion engine, SAE 1999-01-1222.

[22] **Akalın, O. and Newaz, G. M.**, 2001. Piston ring-cylinder bore friction modeling in mixed lubrication regime: Part I-Analytical results, ASME Journal of Tribology, **123**, 211-218.

[23] **Akalın, O. and Newaz, G. M.**, 2001. Piston ring-cylinder bore friction modeling in mixed lubrication regime: Part II-Correlation with bench test data, ASME Journal of Tribology, **123**, 219-223.

[24] **Akalın, O. and Newaz, G. M.**, 1998. A new experimental technique for friction simulation in automotive piston ring and cylinder liners, SAE 981407.

[25] **Priest, M., Dowson, D. and Taylor, C. M.**, 2000. Theoretical modelling of cavitation in piston ring lubrication, Proc. Instn. Mech. Engrs., **214** Part C, 435-447.

[26] **Teraguchi, S., Suzuki, W., Takiguchi, M. and Sato, D.**, 2001. Effects of lubricating oil supply on reductions of piston slap vibration and piston friction, SAE 2001-01-0566.

[27] **Sato, O., Takiguchi, M., Aihara, T., Seki, Y., Fujimura, K. and Tateishi, Y.**, 2004. Improvement of piston lubrication in a diesel engine by means of cylinder surface roughness, SAE 2004-01-0604.

[28] **Shin, S., Cusenza, A. and Shi F.**, 2004. Offset crankshaft effects on SI engine combustion and friction performance, SAE 2004-01-0606.

[29] **Dellis, P. and Arcoumanis, C.**, 2004. Cavitation development in the lubricant film of a reciprocating piston–ring assembly, Proc. Instn. Mech. Engrs., **218** Part J, 157-171.

[30] **Hu, Y., Cheng, H. S.,Arai, T., Kobayashi, Y. and Aoyama, S.**, 1994. Numerical simulation of piston ring in mixed lubrication – A nonaxisymmetrical analysis, ASME Journal of Tribology, **116**, 470-478.

[31] **Coyne, J. C., and Elrod, H. G.,** 1970. Conditions for the rupture of a lubricating film. – Part I: Theoretical model. ASME Journal of Lubrication Technology, **92**, 451-456.

[32] **Coyne, J. C., and Elrod, H. G.,** 1970. Conditions for the rupture of a lubricating film. – Part II: New boundary conditions for Reynolds equation. ASME Journal of Lubrication Technology, **93**, 156-167.

APPENDIX A

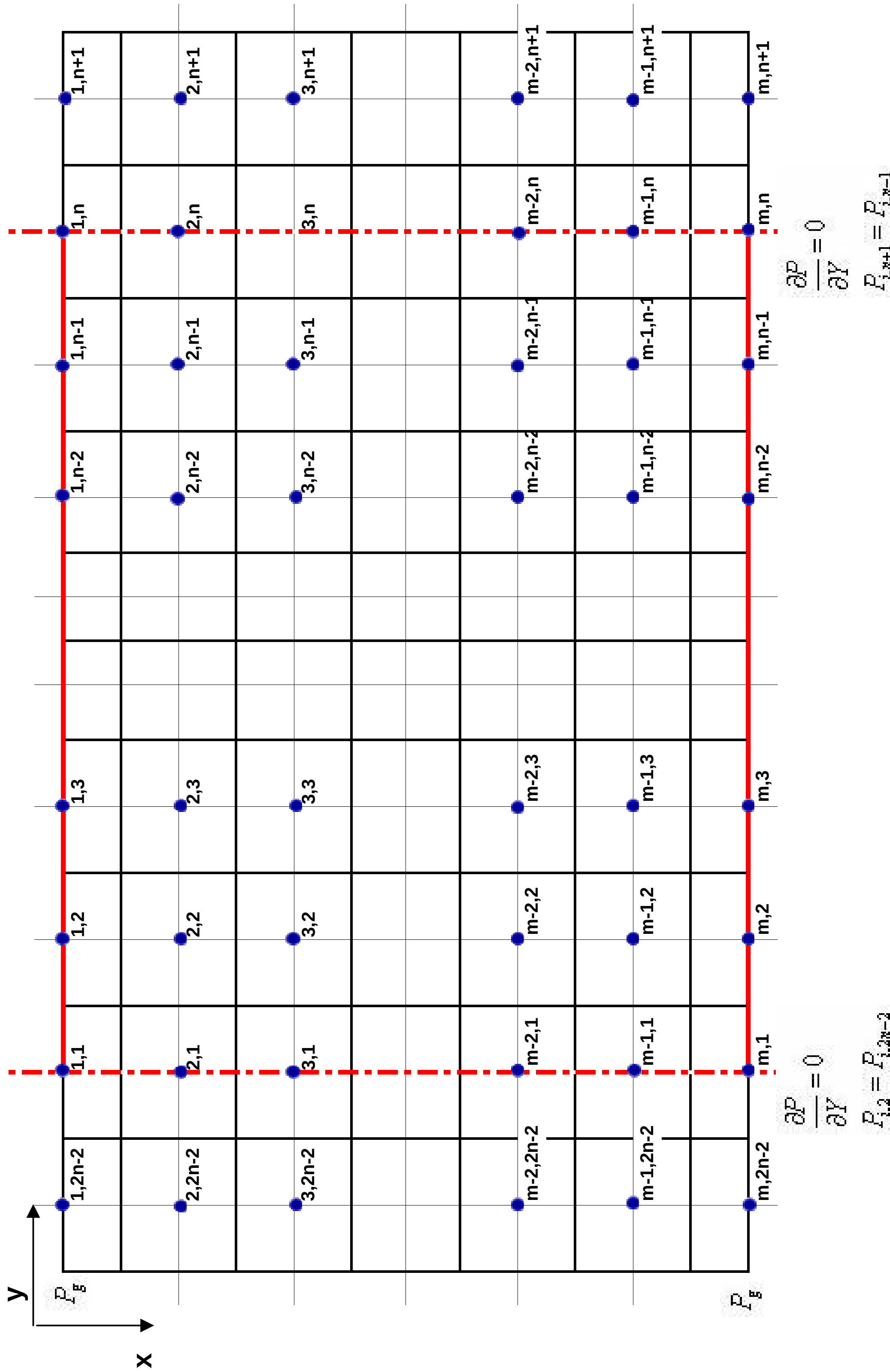

Figure A.1 : General mesh for piston skirt surface

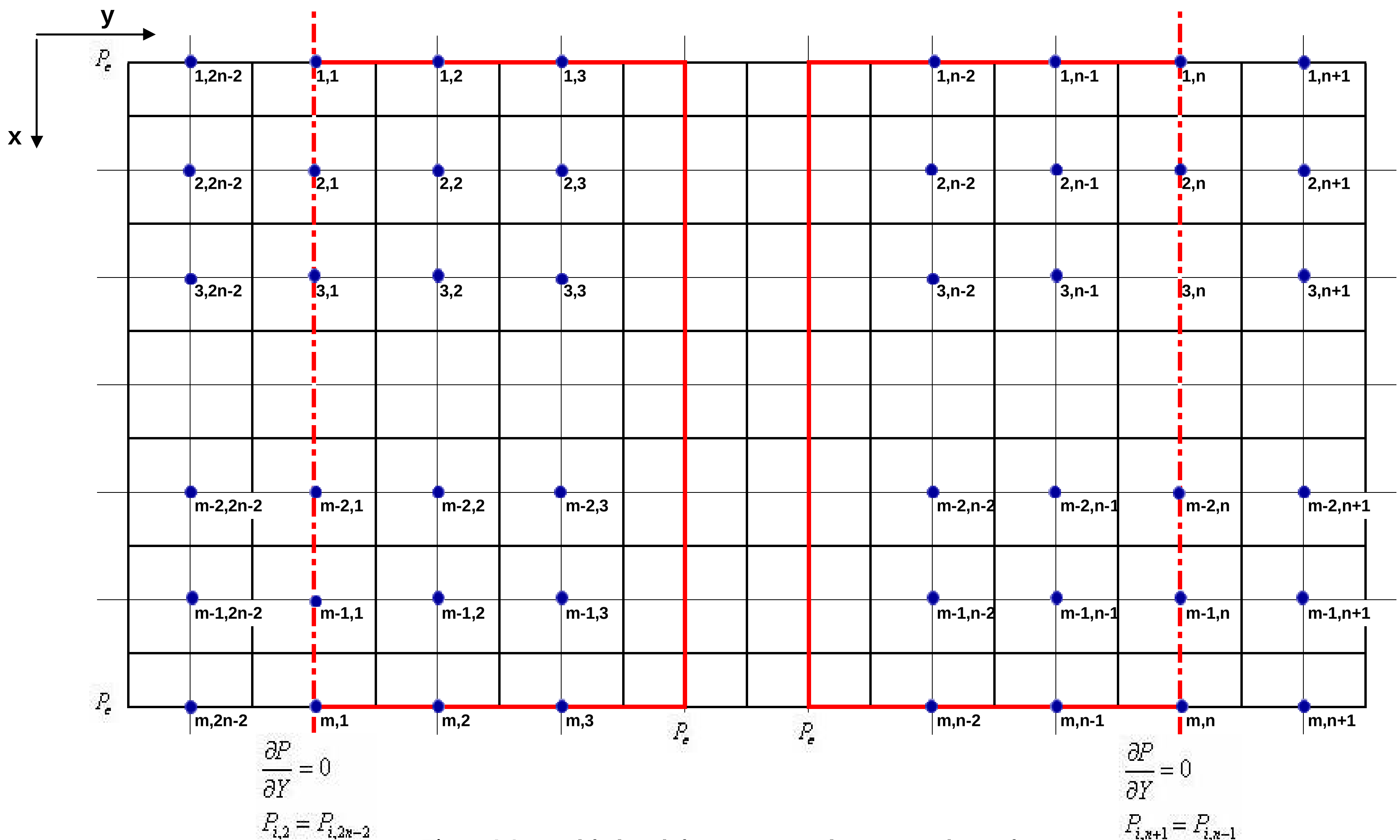

Figure A.2 : Modified mesh for a conventional ICE piston skirt surface

APPENDIX B

Pseude-code for piston secondary motion iteration:

```
et(0) = 0;
det(0) = 0;
eb(0) = 0;
deb(0) = 0;
det(1) = 0;
deb(1) = 0;

errf = 0.01;
errm = 0.01;

k = 0;
for CA = -50:dCA:720
   k = k+1;
   toe = CA*pi/180;
   Up = sin(toe)+0.5*CR/CRL*sin(2*toe)*CR*w;
   Ap = CR*w^2*(cos(toe)-CR/CRL*cos(2*toe));
   ABz = CR*w^2*(cos(toe)-CR/cBM*cos(2*toe));
   ABx = CR*(cBM/CRL-1)*w^2*sin(toe);
   Fg = pg*pi*R^2;

   errffprev = 0;
   errmmprev = 0;
   dummyf = 1;
   dummym = 1;

   dgamma = 0;
   decm = 0;
   dummygamma = 1;
   dummyecm = 1;

   y = 1;

   while max([dummyf;dummym])>0
      y = y+1;
      et(k) = et(k-1)+dt*det(k);
      eb(k) = eb(k-1)+dt*deb(k);
      h = RC+(et(k)-(et(k)-eb(k))*ZZ).*cos(theta2)+delta2;
      H = (1/RC)*h;
      Hsig = (1/sigma)*h;
```

```
HD = (det(k)-(det(k)-deb(k))*ZZ).*cos(theta2);
HD = (1/RC/w)*HD;
P = presdist);
[Fh,Mh] = hydload;
[Ff,Mf] = hydfric;
Frx = (((mp*Ap+Fg-Ff)*CRL+mcon*ABz*cBM)*sin(beta)-
                                mcon*ABx*cBM*cos(beta)-
                                Icon*ddbeta)/(CRL*cos(beta));
FRHS = Fh;
MRHS = Mh;
ddet(k) = (det(k)-det(k-1))/dt;
ddeb(k) = (deb(k)-deb(k-1))/dt;
FLHS = mp*((1-zCM/PL)*ddet(k)+(zCM/PL)*ddeb(k))-Frx;
MLHS = (Ip/PL)*(ddet(k)-ddeb(k))-Mf;
if round(y/2)==y/2;
   dummyf = 0;
   errff = (FRHS-FLHS)/abs(FRHS);
   errmm = (MRHS-MLHS)/abs(MRHS);
   if abs(errff)>errf
      dummyf = 1;
      dgamma = (det(k)-deb(k))/PL;
      decm = det(k)-zCM*dgamma;
      decmprev = decm;
      decm = decm+ff(errff);
      errffprev = errff;
      det(k) = decm+zCM*dgamma;
      deb(k) = decm-(PL-zCM)*dgamma;
   elseif abs(errmm)>errm
      dummym = 1;
      dgamma = (det(k)-deb(k))/PL;
      decm = det(k)-zCM*dgamma;
      dgammaprev = dgamma;
      dgamma = dgamma+fm(errmm);
      errmmprev = errmm;
      det(k) = decm+zCM*dgamma;
      deb(k) = decm-(PL-zCM)*dgamma;
   end
else
   dummym = 0;
   errff = (FRHS-FLHS)/abs(FRHS);
   derrff = (errffprev-errff)/errff;
   errmm = (MRHS-MLHS)/abs(MRHS);
   derrmm = (errmmprev-errmm)/errmm;
   if abs(errmm)>errm
      dummym = 1;
      dgamma = (det(k)-deb(k))/PL;
      decm = det(k)-zCM*dgamma;
      dgammaprev = dgamma;
      dgamma = dgamma+fm(errmm);
      errmmprev = errmm;
```

```
            det(k) = decm+zCM*dgamma;
            deb(k) = decm-(PL-zCM)*dgamma;
         elseif abs(errff)>errf
            dummyf = 1;
            dgamma = (det(k)-deb(k))/PL;
            decm = det(k)-zCM*dgamma;
            decmprev = decm;
            decm = decm+ff(errff);
            errffprev = errff;
            det(k) = decm+zCM*dgamma;
            deb(k) = decm-(PL-zCM)*dgamma;
         end
      end
   end
   det(k+1) = det(k);
   deb(k+1) = deb(k);
end
```

APPENDIX C

Flow chart for the MATLAB code :

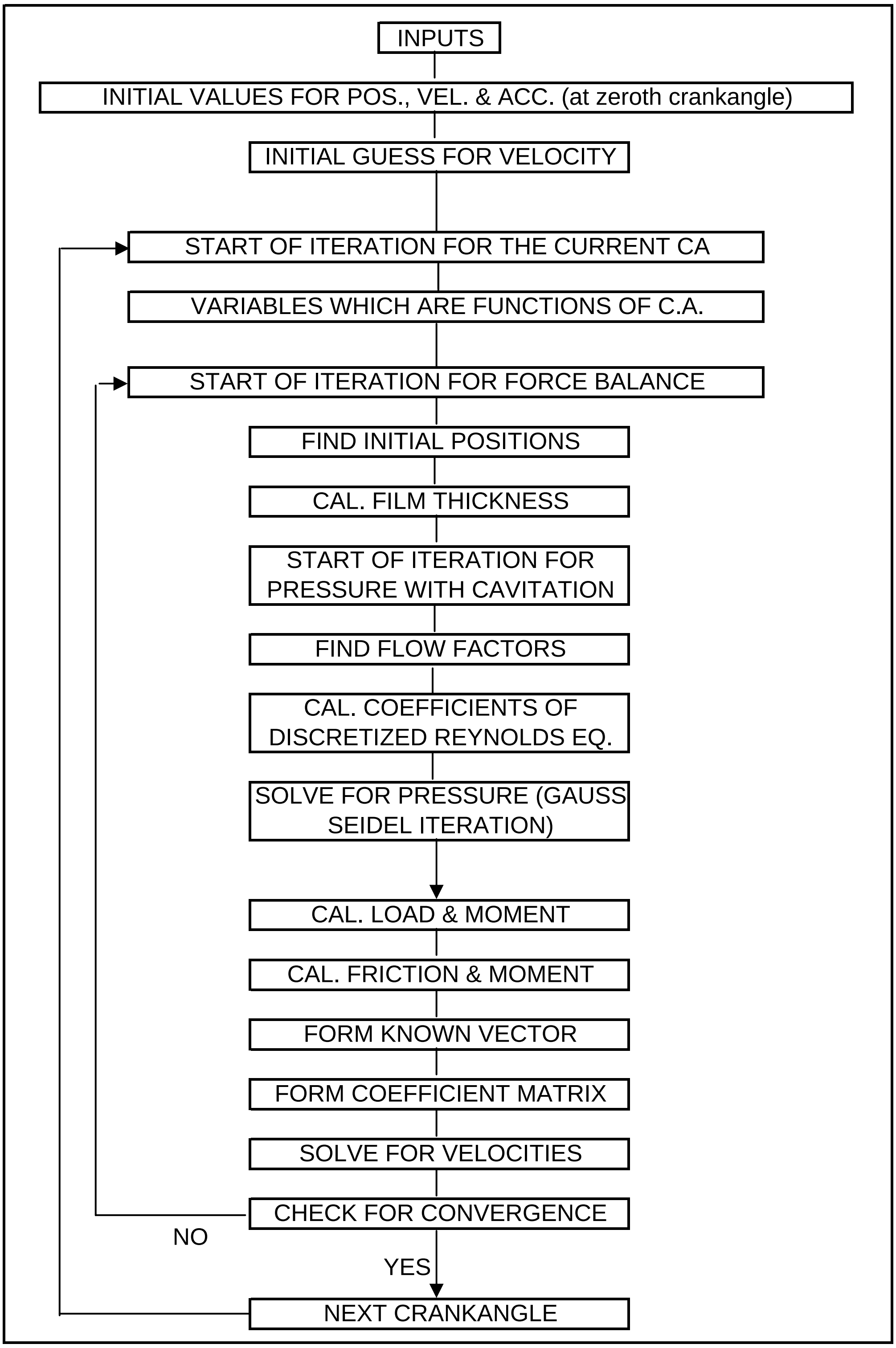

Figure C.2 : Flow chart for the MATLAB code

CURRICULUM VITAE

The author was born in İzmit, in 1980. He graduated from Kadıköy Anadolu Lisesi in 1999. He had his B.Sc. education on mechanical engineering at Middle East Technical University in 1999-2003 and M.Sc. education on automotive engineering at Istanbul Technical University in 2003-2006.